**Transition-Metal doped Titanate Nanowire Photocatalysts Boosted by Selective Ion-Exchange induced Defect Engineering**

Xingxu Lu[a,b], Fangyuan Liu[b], Yanliu Dang[b], Meilin Li[c], Mingyue Ruan[a], Mudi Wu[a], Chunxiang Zhu[a,b], Tomoyasu Mani[c], Steven L. Suib[b,c], Pu-Xian Gao[a,b,*]

[a] Department of Materials Science and Engineering, University of Connecticut, Storrs, CT 06269-3136, USA

[b] Institute of Materials Science, University of Connecticut, Storrs, CT 06269-3136, USA

[c] Department of Chemistry, University of Connecticut, Storrs, CT 06269-3060, USA

[*]Email: puxian.gao@uconn.edu

**KEYWORDS**: Titanate nanowires; Ion-exchange; Defect engineering; Adsorption; Photocatalysis; Dyes.

**ABSTRACT**

Defect engineering through elemental doping is an efficient way to boost the performance of semiconductor photocatalysts. Herein, transition-metal (TM) doped titanate nanowires (TNWs) were prepared *via* ion-exchange over the titanate precursors and demonstrated for the Rhodamine B (RhB) degradation under ultraviolet (UV) light irradiation. The ion-exchange of selective ions ($V^{5+}$, $Cr^{3+}$, $Ni^{2+}$, and $Zn^{2+}$) with protons from pristine TNWs resulted in the hierarchical meso-porosity of nanowires with large pores of ~5-20 nm by TM doping and small pores of ~3.6-4.5 nm inherited from pristine TNWs, which facilitates the mass transfer while maintaining high surface area and active sites. Meanwhile, the TM intercalation partially reduces the $Ti^{4+}$ to $Ti^{3+}$ and narrows the optical bandgap, which, together with oxygen vacancies and superoxide radicals from pristine TNWs, enhance the adsorption and photocatalytic degradation performance of RhB. This work helps to elucidate the effects of transition-metal doping and provides a rational strategy towards high performance titanate-based photocatalysts for efficient and sustainable wastewater treatment.

## 1. INTRODUCTION

Titanium dioxide ($TiO_2$) based photocatalysts possess attractive properties such as low cost, biocompatibility, suitable band-edge positions, and exceptional photo-corrosion resistance [1-3]. Polymorphs of $TiO_2$, including anatase, rutile and brookite, have been extensively studied in the past decades for photocatalytic $H_2$ generation [4, 5], $CO_2$ reduction [6, 7], water purification [8, 9] and recovery of precious metals [10], etc. However, due to the large bandgap energy (3.0-3.5 eV), pristine $TiO_2$ is only active under UV light, limiting its light utilization efficiency. Meanwhile, the rapid recombination of charge carriers and sluggish kinetics of electron transfer from $TiO_2$ to electrolyte also compromise the overall efficiency of the pristine $TiO_2$ as photocatalysts in practice [11]. To address these bottleneck issues, various strategies have been developed through tuning the microstructures and electronic properties of $TiO_2$-based photocatalysts. Examples include the intrinsic doping of $Ti^{3+}$ centers and oxygen vacancies by creating defective $TiO_2$ nanomaterials [11, 12], and the extrinsic doping by introducing the foreign atoms into the $TiO_2$ frameworks to narrow the optical bandgap and enhance the photocatalytic activity [13-15].

Layered titanates have been developed as the precursors of $TiO_2$ lately and proved to be an ideal class of catalyst supports due to their unique layered structures and abundant ion-exchangeable sites [16, 17]. In the case of protonated titanates, the positive protons ($H^+$) can be readily exchanged by metal cations to form metal titanates. The theoretical cation exchange capacity (CEC) is 9.05 mmol/g for the monovalent layered di-titanate, outperforming other common ion exchange materials,

such as clays, zeolites, and zirconium phosphate with CECs in a range of ~0.25-0.6 mmol/g [18-20]. The high surface area and rich cation-exchangeable sites allow atomically dispersed metal cations in the titanate lattices, achieving high metal loading and dispersion. Meanwhile, the abundant defects in the framework of the titanate nanomaterials also help to reduce the energy bandgap by creating additional energy states and generate additional active sites for adsorption and catalytic reactions [17, 21]. Due to the rising environmental concerns of the aqueous contaminants such as pesticides, pharmaceuticals, organic dyes, etc., layered titanate nanomaterials have been extensively studied in the past decade as adsorbers and photocatalysts for water purification due to their high surface area and promising photocatalytic activity [8, 22-24]. For example, Xiong *et al.* [25] reported that the simultaneous adsorption and photocatalytic reaction can promote the degradation of methylene blue over the titanate nanotubes (TNTs), which was not observed from the $TiO_2$ reference. Meanwhile, great efforts have been devoted to improving adsorption capacity and photocatalytic degradation efficiency of the titanate nanomaterials. However, most of the work has been focused on modifying the titanate nanomaterials by using different alkali solutions [26] [27] or creating hybrid composites by combining secondary materials, such as reduced graphene oxide [28], $SiO_2$ [8] and activated charcoal [29]. Comprehensive understanding of the interactions and synergy between the adsorption behavior and photocatalytic activity of the titanate and $TiO_2$ based photocatalysts are still lacking.

In this work, pristine titanate nanowires (TNWs) were prepared via a low-temperature

hydrothermal method by using $TiCl_3$ as the titanium precursors, $H_2O_2$ as the oxidant, and hydrochloric acid as the pH controller [30]. The alkali-free hydrothermal process resulted in protonated TNWs ($H_2Ti_2O_5 \cdot H_2O$). Subsequently, eight transition meal elements, namely V, Cr, Mn, Fe, Co, Ni, Cu and Zn, were intercalated into the layered TNWs through a facile ion-exchange process, and the organic dye removal efficiency was examined by the adsorption and photocatalytic degradation of RhB in aqueous solution. Detailed materials characterization and comprehensive performance evaluation reveal that the selective exchange of V, Cr, Ni and Zn ions have resulted in the amorphous structured transition meal-doped titanate catalysts that outperformed the other samples due to the high surface areas with hierarchical mesoporous networks, narrower energy bandgaps, abundant $Ti^{3+}$ centers, oxygen vacancies, and superoxide radicals. To the best of our knowledge, this is the first time that titanate nanomaterials synthesized by the alkali-free hydrothermal method were reported for the photocatalytic degradation of contaminants in aqueous solutions. The novel synthesis procedures avoid the high temperature and pressurized conditions as well as the additional acid washing steps to remove the $Na^+$ or $K^+$ ions from the titanates prepared via the conventional alkali-based hydrothermal process [22, 31]. The comprehensive characterization and evaluation of the transition metal ion doped TNWs further elucidates the structural-performance relationships in the titanate-based photocatalysts and shall shed light to the development of novel wastewater treatment technologies.

## 2. Experimental

### 2.1. Preparation of TNWs

The protonated titanate nanowires (TNWs, $H_2Ti_2O_5 \cdot H_2O$) were prepared using a low-temperature and alkali-free hydrothermal method [30]. Generally, 10.5 mL hydrochloride acid (HCl, 37%, Sigma-Aldrich), 9 mL titanium (III) chloride ($TiCl_3$, 20% w/v solution in 2M HCl acid, Acros Organics™) and 45 mL hydrogen peroxide ($H_2O_2$, 30% w/w in $H_2O$, Sigma-Aldrich) were mixed with 555 mL deionized (DI) water in a 1000 mL beaker. The beaker was covered by parafilm with a small outlet for gas release, and the hydrothermal synthesis was carried out at 90 °C with magnetic stirring until the solution color turned from deep red to yellow with no bubbles emerging. Subsequently, the TNWs were collected and rinsed with DI water by centrifugation for 5 times, and finally dried in oven at 90 °C overnight. Anatase $TiO_2$ nanowires were prepared by annealing the TNWs at 500 °C in air for 2 hours.

### 2.2. Preparation of transition-metal doped photocatalyst

The transition metals were loaded onto the TNWs via an ion-exchange process [32, 33] using the following transition metal salts as precursors: Ammonium metavanadate ($NH_4VO_3$, Sigma-Aldrich), Chromium(III) nitrate nonahydrate ($Cr(NO_3)_3 \cdot 9H_2O$, Sigma-Aldrich), Manganese(II) nitrate tetrahydrate ($Mn(NO_3)_2 \cdot 4H_2O$, Acros Organics™), Iron(III) nitrate nonahydrate ($Fe(NO_3)_3 \cdot 9H_2O$, Sigma-Aldrich), Cobalt(II) nitrate hexahydrate ($Co(NO_3)_2 \cdot 6H_2O$, Acros Organics™), Nickel(II) nitrate hexahydrate ($Ni(NO_3)_2 \cdot 6H_2O$, Sigma-Aldrich), Copper(II) nitrate trihydrate ($Cu(NO_3)_2 \cdot 3H_2O$, Acros Organics™), Zinc nitrate hexahydrate ($Zn(NO_3)_2 \cdot 6H_2O$,

Acros Organics™). Standard aqueous solution of the transition-metal salts were prepared with a concentration of 1 gram metal element per liter (1 g/L) in 20 mL vials, respectively, and 0.5 g of TNWs was added into the solutions. The vials were capped and sonicated for 30 min to enhance the contact between the nanomaterials and solution, and then the ion-exchange was conducted at 80 °C for 12 h. The ion-exchanged TNWs were collected by centrifugation and washed for 5 times in DI water to remove any residue metal cations, and finally dried at 90 °C overnight. The anatase nanowires were treated in the same way as reference [34].

**2.3. Materials Characterization**

The X-ray diffraction (XRD) of the catalysts were conducted on a Bruker D2 X-ray diffractometer (Cu Kα, 30 kV, 10 mA). The calculation of the degree of crystallinity is obtained by a deconvolution in Gaussian curves. The degree of crystallinity is the ratio of the sum of the deconvoluted crystalline part over the sum of the crystalline and the amorphous deconvoluted parts. The morphology, composition, and structure of the nanoarray catalysts were characterized using a high-resolution scanning transmission electron microscope (HR-STEM) (FEI Talos F200X S/TEM, 200 kV). Electron energy loss spectroscopy (EELS) was performed using a Gatan Image Filter Quantum SE/963 P system which equipped on the STEM with an energy resolution (full-width of half maximum) of 0.95 eV over a HR-STEM (Titan Themis, 300kV TEM/STEM). The X-ray photoelectron spectroscopy (XPS) were performed with a Quantum 2000 Scanning ESCA Microprobe, using a monochromatic Al Kα X-ray source. The shift of binding energy due to relative surface charging was calibrated

using the C 1s level at 284.8 eV as an internal standard [35].

The specific surface areas were measured by the Brunauer–Emmett–Teller (BET) method from the nitrogen adsorption–desorption isotherms measured at 77 K using a Micromeritics ASAP 2020 Automatic Chemisorption Analyzer. The sample was degassed at 150 °C for 4 h under vacuum prior to the BET determination [36]. Raman spectra were taken with a Renishaw 2000 Raman microscope with an Ar+ ion laser (514 nm) as the excitation source. Ultraviolet−visible diffusive reflectance spectra (UV−vis DRS) of the samples were obtained relative to the reflectance of a standard ($BaSO_4$) using a UV/Vis spectrophotometer (Shimadzu UV 2450) equipped with a diffuse reflectance sampling accessory [37]. The samples were pressed into pellets of 2 g of $BaSO_4$ and 50 mg of the powder samples. The band gap evaluation was performed using the Tauc method. Electron paramagnetic resonance (EPR) analysis was performed on a Bruker EMXnano spectrometer at room temperature, operating at the X band (~9.8 GHz). The magnetic field was modulated at 100 kHz and the *g* value was determined from the precise frequency and magnetic field values.

**2.4. Adsorption Experiments**

For the adsorption kinetic experiments, 20 mg of the photocatalyst powders were added into 100 mL RhB aqueous solutions with an initial concentration of 5 mg/L. All the adsorption experiments were carried out in the dark to avoid the influence of any photocatalytic reactions. The suspensions were kept in conical flasks and agitated by a magnetic stirring plate running at 500 rpm and 25 °C. The aliquots were collected from the solutions at appropriate time intervals and then immediately centrifuged for

5 min at 10,000 rpm to separate solid particles. The residual RhB concentrations in the solutions were determined by absorbance measurements using a UV-vis-NIR spectrophotometer (Lambda 900, PerkinElmer) using a standard calibration curve.

For the adsorption isotherm experiments, the experimental procedure employed in the kinetic experiments was applied with varied initial concentrations of RhB at 1, 2, 5, 10 and 20 mg/L, respectively. The time for adsorption equilibrium was set at 240 min to achieve sufficient adsorption in the kinetic experiments.

**2.5. Photocatalytic Performance**

Considering the fact that the $TiO_2$-based photocatalysts are mostly active in the range of UV range, the photocatalytic degradation of RhB was conducted using a Luzchem ring illuminator equipped with UV light (356 nm, 220 W). The transition-metal doped TNW and anatase $TiO_2$ photocatalysts as well as the commercial P25 $TiO_2$ powder (50 mg) were dispersed in 100 mL RhB aqueous solutions (5 mg/L) in a quartz flask. In order to avoid the impacts of photon adsorption and light scattering of the photocatalyst suspensions on the photocatalyst activity evaluation [38-40], all the tests were conducted with the aqueous suspension agitated by magnetic stirring of 500 rpm in the UV ring illuminator, which can guarantee the sufficient mixing of the aqueous solution and catalyst suspension as well as an equal "optical thickness". It should also be noted that the magnetic field created by the magnetic stirring plate beneath the quartz flask may also influence the photocatalytic performance of the catalysts. When moving in the magnetic field, the electrons and holes are subjected to the Lorentz force in opposite directions according to the left-hand rule, and therefore, which

facilitates the photogenerated electron−hole pairs in the moving photocatalysts [41, 42]. However, due to the lack of the magnetic field profiles and the equivalent testing conditions of all the photocatalysts, the influence by the magnetic field created by the magnetic stirring plate was ignored in the present work. Before the photocatalytic reactions, the suspensions were kept in the dark for 30 min to reach the adsorption and desorption equilibria, and then the UV light was turned on to initiate the photocatalytic reactions. During the tests, 2 mL of the suspensions were collected at the designed times and quickly centrifuged at 10,000 rpm for 5 min to separate the solution and solid powders. The concentration of RhB was measured by UV-vis-NIR absorption spectroscopy in the same way as in the adsorption experiments. The stabilities of the photocatalysts were also evaluated by conducting the simultaneous adsorption and photocatalytic degradation experiments for extended time. Detailed testing procedures are presented in **Table S1** in the supporting information, and the evolution of residue RhB concentrations were recorded along the reaction time.

## 3. Results and Discussion

### 3.1. RhB Removal Efficiency

The RhB removal efficiency of the transition-metal doped TNWs (M-TNW) are compared with the commercial P25 $TiO_2$ powder in **Fig. 1**. The RhB removal tests were conducted in two steps: the samples were kept in the dark for 30 min at first to reach adsorption and desorption equilibrium, and then exposed to the UV light irradiation ($\lambda$= 356 nm) for photocatalytic degradation. As shown in **Fig. 1a**, the pristine TNWs exhibit a removal efficiency with ~65% RhB removed during the

adsorption step, while the P25 $TiO_2$ only adsorbed 15% of the RhB due to the lack of the interlayer structures and low surface area [43]. The transition metal doping modified the TNWs in three ways according to their RhB adsorption performance. For V, Cr, Ni and Zn doped samples, more than 80% of RhB was quickly removed from the solution in the first 30 min, suggesting these dopant elements can greatly enhance the adsorption efficiency of the TNWs. For the Fe, Co and Cu doped samples, only 30~50% of the RhB can be removed, indicating a lower adsorption capacity than the pristine TNWs. Finally, the Mn-TNW shows limited adsorption capacity with only 18% of RhB removed. When the UV light was turned on at 30 min, the photocatalytic degradation of RhB was initiated. The RhB removal efficiency of the V, Cr, Ni and Zn doped samples quickly reached 95% in 10 min, demonstrating the excellent photocatalytic reactivity. The pristine TNWs, commercial P25 $TiO_2$ and Cu-TNW showed moderate RhB degradation rates and achieved 99% RhB removal after 85 min, while the Fe-TNW sample showed a low RhB removal rate and reached 99% RhB removal after 120 min. The Co-TNW sample showed an even lower photocatalytic degradation activity than Fe-TNW with only 80% of the RhB removed from the solution after 150 min. Finally, the RhB concentration remained almost unchanged for the Mn doped TNWs during the entire process, indicating a negligible photocatalytic activity of the Mn-TNW sample. **Fig. 1b** compares the contributions from adsorption and photocatalytic degradation to the overall RhB removal at 60 min.

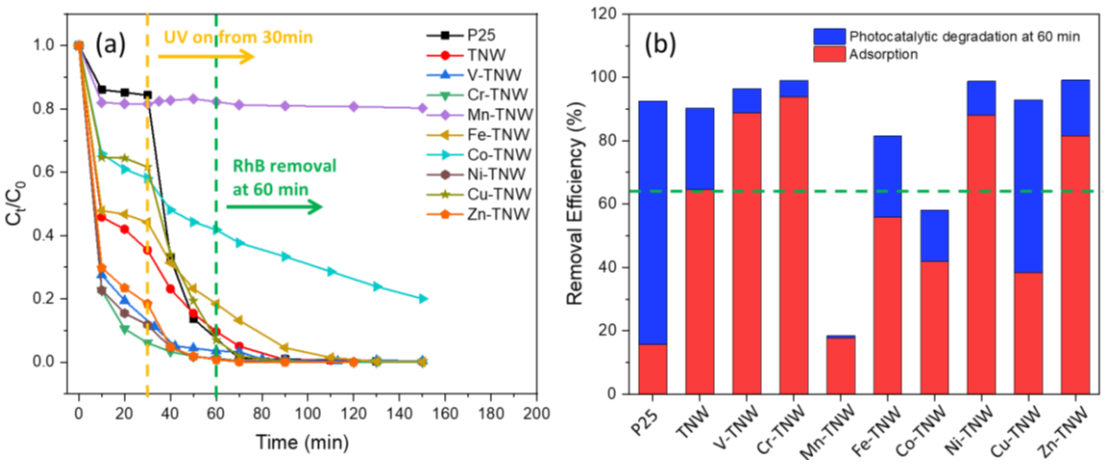


**Fig. 1.** Adsorption and photocatalytic degradation of RhB from aqueous solutions over the pristine and transition-metal doped TNWs with commercial P25 $TiO_2$ as reference: (a) evolution of RhB concentration along the reaction time and (b) the contributions from adsorption (red bar) and photocatalytic degradation (blue bar) to the RhB removal at 60 min. Samples were kept in dark for 30min followed by UV irradiation at $\lambda$= 356 nm under magnetic stirring at room temperature.

The V, Cr, Ni and Zn doped samples outperform the pristine TNW and commercial P25 for RhB removal, indicating the promotional effects of these elements as dopant to the TNWs. Meanwhile, the transition meal doped anatase $TiO_2$ nanowires (M-ANT) were also evaluated for the RhB degradation under the same conditions, and the evolution of RhB concentration along the reaction time is displayed in **Fig. S1**. Compared with the titanate-based photocatalysts, the anatase-based samples showed negligible RhB adsorption capacity and low photocatalytic activity towards RhB degradation, and none of the anatase-based samples achieved complete RhB removal under the UV light irradiation for 120 min. The compromised adsorption ability and photocatalytic activity of the anatase-based photocatalysts result from the change in

the microstructures of the nanomaterials during the annealing treatment. Our previous research revealed that the protonated titanates transform into anatase $TiO_2$ upon thermal annealing, followed by the destruction of the interlayer structures, loss of ion-exchangeable sites and decrease in specific surface area [30]. The RhB degradation experiments demonstrate the varied dopant effects on the TNW-based photocatalysts. The following sections will then be focused on elucidating how transition meal elements modified the microstructure and properties of the TNW nanomaterials and the mechanisms for the varied adsorption behaviors and photocatalytic activities.

### 3.2. Structure, Morphology and Porosity

The evolution in the structures and morphologies of the TNWs before and after the introduction of the transition metal dopants are presented in **Fig. S2-S4** and **Fig. 2**. The bright field (BF) TEM images in **Fig. S2a** reveal the distinctive nanowire structures of the pristine TNWs. When the transition metal dopants were introduced through ion-exchange, the TNW morphology changed differently with respect to different transition metal ions. On the one hand, for the V-TNW, Cr-TNW, Ni-TNW and Zn-TNW samples shown in **Fig. S2b**, **c**, **g** and **i**, respectively, no obvious morphology changes were observed after ion-exchange. On the other hand, the incorporation of Mn, Fe, Co and Cu brought significant changes to the TNW morphologies. For the Mn-TNW (**Fig. 2Sd**), Co-TNW (**Fig. S2f**) and Cu-TNW (**Fig. S2h**) samples, secondary nano-flakes were formed on the TNWs after ion exchange, resulting in a 3-dimensional (3D) nanostructure. The Fe-TNWs (**Fig. S2e**) are

decorated with nano-bundle clusters on the surface of the nanowires. Clearly the intercalation of the selective ions in $Mn^{2+}$, $Fe^{2+}$, $Co^{2+}$ and $Cu^{2+}$ caused more drastic changes to the pristine TNW framework than that of $V^{5+}$, $Cr^{3+}$, $Ni^{2+}$ and $Zn^{2+}$, which might be related to their relatively larger exchanged ionic radii distribution [44].

Interestingly, the observed morphologies changes can be correlated to the varied RhB adsorption properties and photocatalytic activities of these samples. The XRD patterns and crystallinities of the transition-metal doped TNWs are displayed in **Fig. S3**. As shown, the pristine TNWs exhibit broad and weak XRD signals which could only be detectable after being amplified by 20 times, indicating the amorphous nature of these TNWs [30]. After the intercalation of transition metal cations through ion-exchange, anatase (JCPDS 21-1272), rutile (JCPDS 21-1276) and slight amounts of brookite (JCPDS 29-1360) $TiO_2$ were formed, and the crystallinity of the TNWs increases in different degrees according to the dopant elements. Similar to the variation in the morphologies, the transition-metal doped TNWs can be categorized into two groups, the V, Cr, Ni and Zn doped samples with low crystallinity of < 90%, and the Mn, Fe, Co and Cu doped samples with high crystallinity of 93-99%. The higher crystallinities suggests that Mn, Fe, Co and Cu dopants bring more drastic changes to the TNW microstructures, which enhance the crystallinity but result in the lower adsorption capacity and compromise photocatalytic activity compared to the V, Cr, Ni and Zn doped samples. The formation of the nano-flake and nano-bundle clusters on the Mn, Fe, Co and Cu doped TNWs does not result in phase segregation, and no oxides of these metal elements were observed in the XRD or Raman patterns

(**Fig S4**) of these ion-exchanged samples.

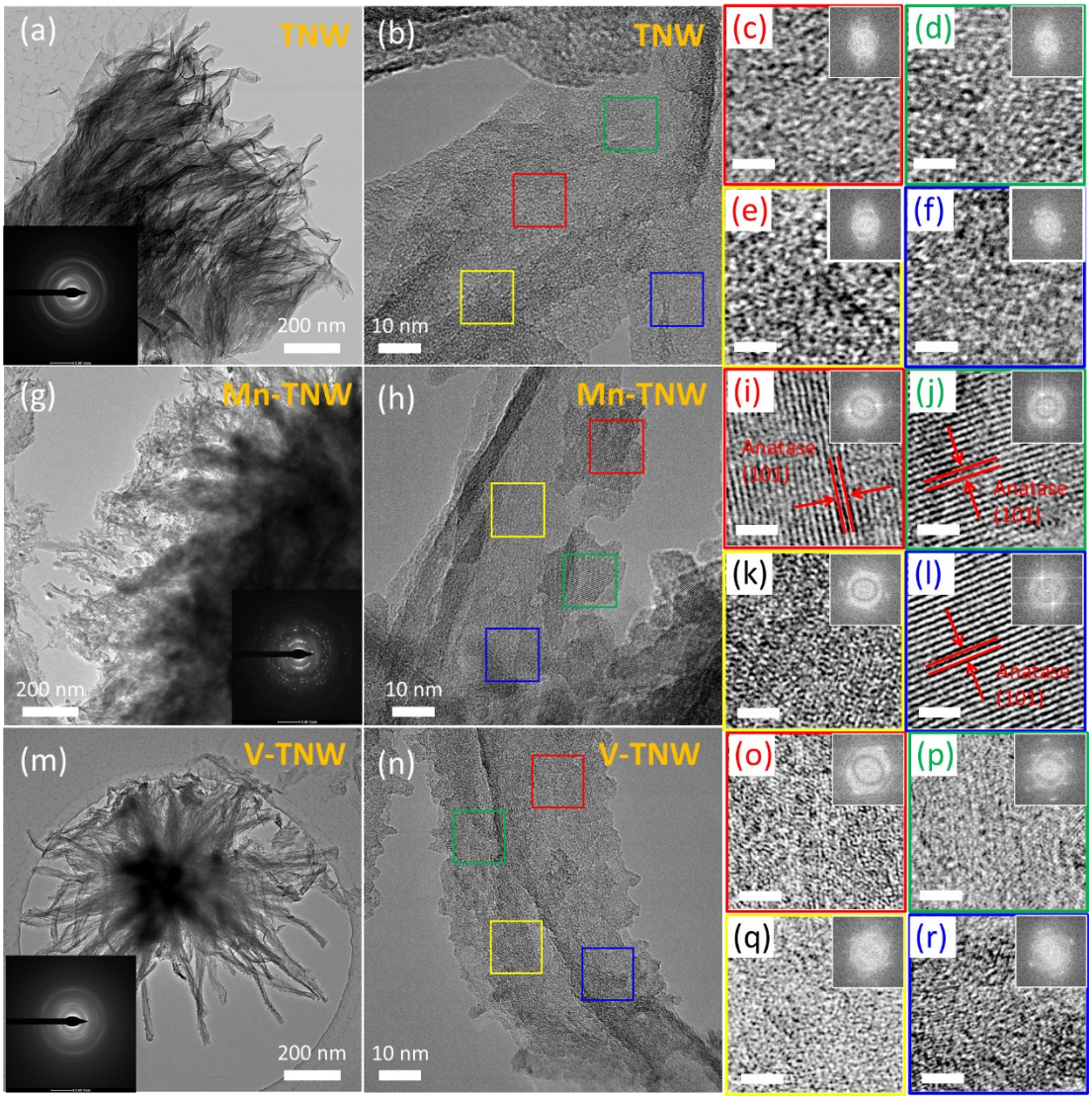


**Fig. 2.** The BF TEM images with SAED patterns inserts and the HRTEM images with FFT patterns inserts of the (a-f) pristine TNW, (g-l) Mn-TNW and (m-r) V-TNW. The lattice images on the right row are the enlarged boxed areas with the corresponding colors in HRTEM images in the middle row. The unmarked scale bars are 1 nm.

Detailed structure and morphology characterization of three representative samples, namely the pristine TNW, Mn-TNW and V-TNW, are displayed in **Fig. 2**. As shown, the pristine TNWs (**Fig. 2a-b**) and V-TNWs (**Fig. 2m-n**) exhibit distinctive nanowire structures with rough surfaces and diffusive selective area electron diffraction (SAED)

patterns (**Fig. 2a** and **m** inserts). The enlarged HRTEM images and the inserted Fast Fourier Transform (FFT) patterns also reveal the disordered microstructures in both samples, which agrees with the low crystallinities determined by the XRD in **Fig. S3b**. On the other hand, the introduction of Mn resulted in the secondary branched structures on the TNWs, as displayed in **Fig. 2h**. Detailed analysis of the lattice images and FFT patterns of the enlarged HRTEM images (**Fig. 2i-l**) reveals that the secondary branch structures are highly crystalline that can be indexed according to the anatase (101) planes (**Fig. 2i**, **j**, and **l**), while the prime TNW still maintains the disordered microstructures (**Fig. 2k**).

The modifications in microstructures of the TNWs brought by transition metal doping are not only revealed by the evolutions in morphology and crystallinity, but also reflected in the changes in the specific surface area and porosity. The BET isotherms and BJH pore-size distributions of the pristine and ion-exchanged TNWs are presented in **Fig. 3** and **Table 1**. The $N_2$ adsorption-desorption isotherms (**Fig. 3a**) of both the pristine and the transition-metal doped TNWs exhibit a type IV feature with a type H3 hysteresis loop, indicating the samples are mesoporous with slit shaped pores formed by agglomerates of particles with non-uniform size and shape [45-47]. Despite the similar shape of the BET isotherms, the pore-size distribution of the ion-exchanged TNWs are quite different. As presented in **Fig. 3b**, the pristine TNWs exhibit a distinct pore size distribution in the range of 3-4.5 nm, which suggests the mesoporous nature of the protonated titanate nanomaterials. Upon the introduction of transition metal cations, the pore size distribution profiles can be categorized into two

groups. The V, Cr, Ni and Zn doped samples retain the mesopores of 3-4.5 nm, but also develop large pores in the range of 5-20 nm. However, for the Mn, Fe, Co and Cu doped samples, the mesopores of 3-4.5 nm are destroyed, and only the large pores of 5-20 nm exist in the nanomaterials. The different pore size distribution patterns agree with the previous conclusion, that the introduction of V, Cr, Ni and Zn maintains the microstructure and mesopores of the TNWs, and therefore possess high specific surface area and abundant ion-exchangeable sites. Meanwhile the newly developed large mesopores facilitate the mass transfer of the dye molecules, which are beneficial for the efficient adsorption of RhB from the bulk aqueous solution. The intercalation of Mn, Fe, Co and Cu, however, destroyed the innate mesoporous structures in the TNWs (3-4.5 nm), resulting in low specific surface area and ion-exchanging capacity, which compromises the RhB adsorption ability. All these results suggest that the selective ion-exchange of the transition metal elements brings varied modifications to the microstructures of the TNWs, which further alters the adsorption and photocatalytic activity of the TNW-based photocatalysts.

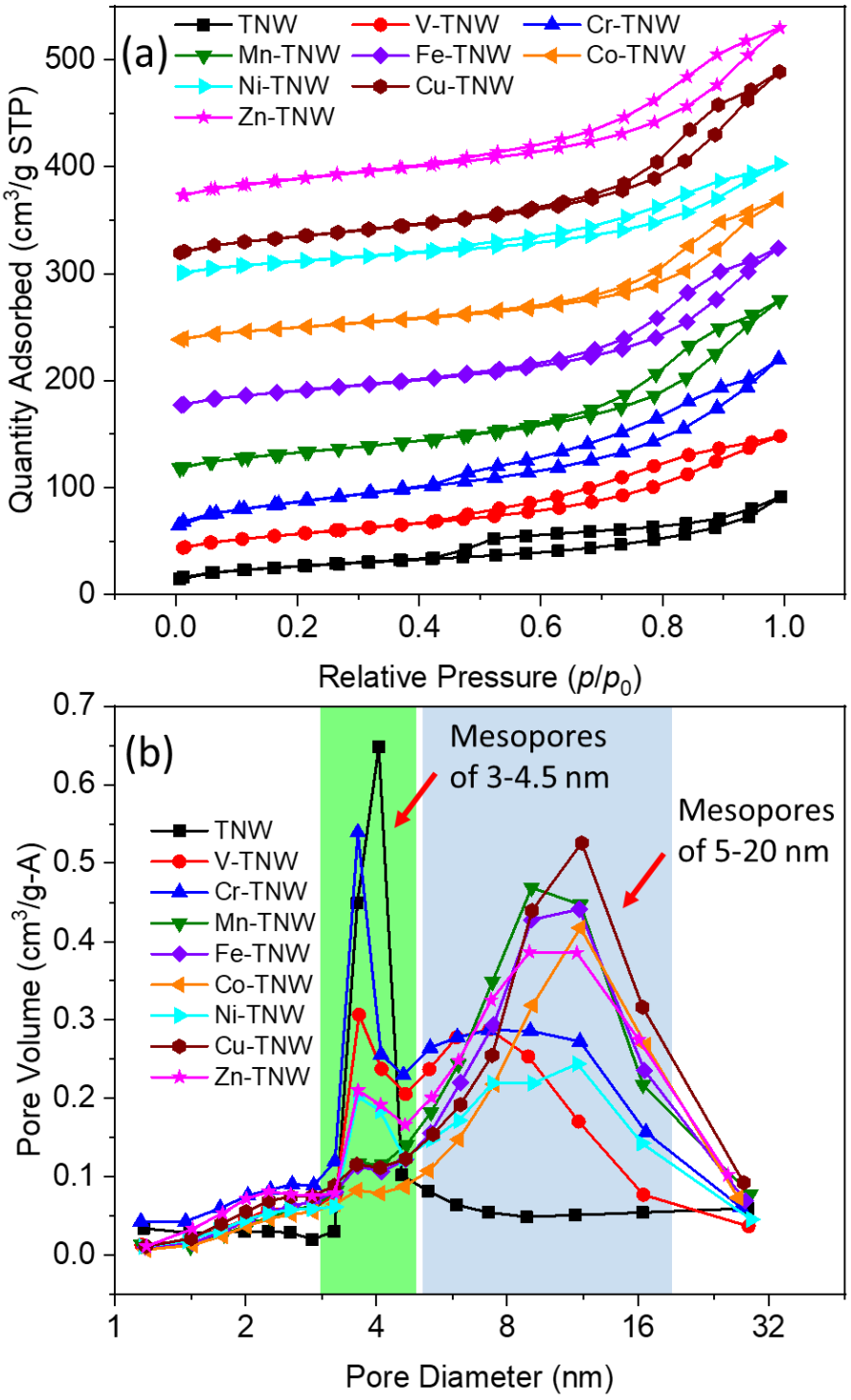


**Fig. 3.** (a) $N_2$ adsorption−desorption isotherms, and (b) pore-size distributions of the pristine and transition-metal doped TNWs.

**Table 1.** Summary of the physio-chemical properties of the transition-metal doped TNWs in this work.

| Sample ID | Bandgap [a] (eV) | $S_{BET}$ [$m^2/g$] | Pore size [nm] | Pore volume [$cm^3/g$] | Crystallinity [b] | Surface species content (at.%) [c] | | | | | |
|---|---|---|---|---|---|---|---|---|---|---|---|
| | | | | | | $Ti^{3+}$ | $Ti^{4+}$ | $O^{\alpha}$ | $O^{\beta}$ | $O^{\gamma}$ | $O^{\delta}$ |
| TNW | 2.92 | 129 | 4.05 | 0.13 | | 0 | 100 | 19.8 | 43.6 | 26.5 | 10.1 |
| V-TNW | 2.69 | 130 | 3.65 | 0.19 | 74% | 39.0 | 61.0 | 35.1 | 42.8 | 17.5 | 4.6 |
| Cr-TNW | 2.87 | 206 | 3.63 | 0.26 | 51% | 32.6 | 67.4 | 37.6 | 35.2 | 14.3 | 13.0 |
| Mn-TNW | 3.35 | 118 | 9.11 | 0.26 | 96% | 8.4 | 91.6 | 5.6 | 75.8 | 5.6 | 13.0 |
| Fe-TNW | 3.12 | 110 | 9.11 | 0.24 | 99% | 9.6 | 90.4 | 3.4 | 75.7 | 4.9 | 16.0 |
| Co-TNW | 3.22 | 89 | 11.80 | 0.21 | 96% | 8.7 | 91.4 | 1.6 | 77.8 | 5.1 | 15.5 |
| Ni-TNW | 2.98 | 124 | 3.63 | 0.17 | 87% | 22.8 | 77.2 | 16.2 | 63.6 | 14.3 | 5.9 |
| Cu-TNW | 3.14 | 111 | 9.13 | 0.27 | 93% | 10.5 | 89.5 | 3.4 | 70.2 | 4.2 | 22.2 |
| Zn-TNW | 3.03 | 138 | 3.63 | 0.26 | 81% | 16.4 | 83.6 | 12.1 | 67.8 | 13.0 | 7.1 |

[a]: Indirect bandgap.

[b]: Crystallinity determined by XRD.

[c]: Surface species content determined by XPS, $O^{\alpha}$ = lattice oxygen (Ti-O-Ti), $O^{\beta}$ = surface labile oxygen (-OH), $O^{\gamma}$ = superoxide radicals ($O_2^{\bullet -}$) and $O^{\delta}$ = surface adsorbed water oxygen ($H_2O$)

### 3.3. Adsorption Properties

In this section, the adsorption kinetic and isotherms were studied to elucidate the adsorption behaviors and mechanisms of the transition-metal doped TNW samples.

#### 3.3.1. Adsorption Kinetics for the RhB Removal by Ion-exchanged TNWs

The adsorption of RhB over P25, pristine and ion-exchanged TNWs were recorded along the contact time, and the adsorption kinetic data were interpreted using pseudo-first-order (**Eq. 1**) and pseudo-second-order model (**Eq. 2**) as follows [29]:

Pseudo-first-order model

$$\frac{dq_t}{dt} = k_1\left(q_e - q_t\right) \qquad \textbf{(Eq.1)}$$

Pseudo-second-order model

$$\frac{dq_t}{dt} = k_2\left(q_e - q_t\right)^2 \qquad \textbf{(Eq.2)}$$

where $q_e$ and $q_t$ (mg/g) represent the uptakes of RhB when the systems reach equilibrium at time $t$ (min); $k_1$ ($min^{-1}$) and $k_2$ (g/mg/min) are the rate constants of pseudo-first-order and pseudo-second-order model, respectively. The simulated kinetic parameters of RhB adsorption over the different samples using the two models are summarized in **Table 2**. By comparing the $R^2$ values, the pseudo-second-order model can better describe the adsorption kinetics data than the pseudo-first-order model, indicating that the chemical interaction between adsorbate and adsorbent determines the adsorption mechanism [29, 48]. The adsorption kinetics of RhB by different samples are plotted using the parameters from the pseudo-second-order model along the experimental data in **Fig. 4a and b**. As shown, the commercial P25 $TiO_2$ uptake very limited amounts of RhB ($q_{e,exp}$ = 1.495 mg/g,

$q_{e,cal}$ = 1.729 mg/g), and become saturated quickly in 15 min. The pristine TNWs exhibit a moderate RhB adsorption with $q_{e,exp}$ = 8.653 mg/g and $q_{e,cal}$ = 9.268 mg/g, which is ~6 times higher than that of P25 $TiO_2$. After the introduction of the transition metal elements into the TNW matrix, the doping of V, Cr, Ni and Zn further enhance the RhB adsorption to 15-22 mg/g, while the addition of Mn, Fe, Co and Cu decrease the uptakes to 2-6 mg/g.

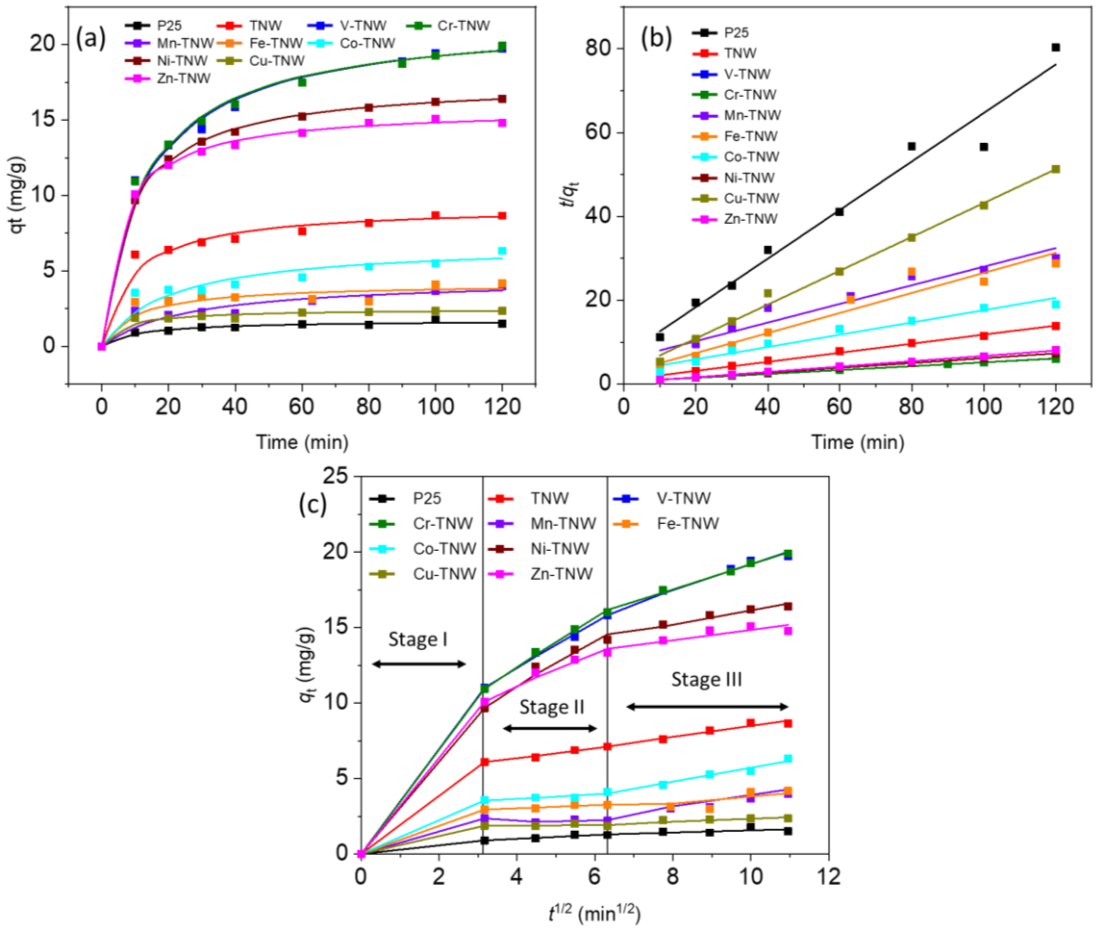


**Fig. 4.** Adsorption kinetics of RhB by P25, pristine and transition-metal doped TNWs: (a) uptakes along the adsorption time and (b) liner plot using the pseudo-second-order model. (c) The intra-particle diffusion model.

In order to further elucidate the adsorption mechanisms and determine the rate-limiting step, the intra-particle diffusion model was employed to analyze the

adsorption kinetic data [49]:

$$q_t = k_i t^{1/2} + C_i \quad \textbf{(Eq. 3)}$$

where $k_i$ is the intra-particle diffusion rate constant and $C_i$ indicates the boundary layer effect of the adsorption. The plot of $q_t$ versus $t^{1/2}$ generally consists of the initial portion and the second portion, which are indicators of the boundary layer effect and intra-particle diffusion, respectively. Previous studies revealed a multi-linearity plot including two or more stages through the adsorption process [50]: Stage I is the external adsorption from the bulk solution to the absorbent surface, which can be instantaneous; Stage II is the gradual adsorption stage, which can be ascribed to the dye diffusion from the absorbent surface to intra-particle active sites, which is controlled by the intra-particle diffusion; Stage III is the final equilibrium stage when the intra-particle diffusion starts to slow down due to saturation of the adsorption sites [51]. The adsorption kinetics using the intra-particle diffusion model ($q_t$ vs. $t^{1/2}$ plot) are displayed along the experimental data in **Fig. 4c**, and the fitted parameters for each stage are summarized in **Table 2**. A good correlation of rate data in this model helps to justify the adsorption mechanisms, and the linear plot of the Stage II allows obtaining the value of $k_4$ and $C_4$. Generally, the smaller value of $C_4$ for Stage II, the greater contribution from intra-particle diffusion, and the adsorption becomes solely governed by intra-particle diffusion if $C_4$ is equal to zero [52]. As illustrated, the samples with enhanced adsorption capacity, including the pristine TNWs, V-TNW, Cr-TNW, Ni-TNW and Zn-TNW, exhibit $C_4$ values in the range of 5-7 mg/g, which are much smaller than the values of 69.1 mg/g [29] and 150-335

mg/g [53] reported in the literature. Therefore, the intra-particle diffusion is the rate-limiting-step that controls the adsorption rates. Moreover, the $q_t$ vs. $t^{1/2}$ plot in **Fig. 4c** reveals that Stage III of the pristine TNW, V-TNW and Cr-TNW samples is less obvious than that of the Ni-TNW and Zn-TNW samples, indicating an intra-particle diffusion controlled period for the pristine TNW and the V and Cr doped samples. This can be explained by the pore size distribution patterns of these samples shown in **Fig. 3b**, that the pristine and V and Cr doped TNWs retain a higher ratio of the mesopores of 3-4.5 nm than the Ni and Zn doped samples. The higher ratio of small mesopores results in a tighter pore structure, which contribute to a longer intra-particle diffusion period in these samples [50].

### 3.3.2. Adsorption Isotherms of RhB on Ion-exchanged TNWs

The equilibrium adsorption isotherm can be obtained by plotting the equilibrium adsorption amount ($q_e$) along the adsorbate concentration ($C_e$) by using RhB aqueous solutions with different initial concentrations. The proper modeling of the adsorption isotherms can help to elucidate the interactions between pollutant and adsorbent [52]. The common two-parameter Langmuir and Freundlich models are used to describe the adsorption isotherms of dyes on the catalysts in this work [28, 54]:

The Langmuir equation basically assumes a homogeneous adsorbent surface where monolayer adsorption occurs:

$$\frac{C_e}{q_e} = \frac{1}{Q_{\max} K_L} + \frac{C_e}{Q_{\max}} \qquad \textbf{(Eq. 4)}$$

where $Q_{max}$ is the maximum adsorption corresponding to monolayer coverage (mg/g) and $K_L$ is the Langmuir equilibrium constant (L/mg).

The Freundlich equation is a purely empirical expression, which implies a heterogeneous adsorption and:

$$\ln q_e = \ln K_F + \frac{1}{n} \ln C_e \quad \textbf{(Eq. 5)}$$

where $K_F$ is the Freundlich constant, and $n$ represents the adsorption intensity. The fitted adsorption parameters and $R^2$ values using the two models are summarized and compared in **Table S2**. Based on the fitted parameters, the isotherms are better depicted by the Langmuir model with higher $R^2$ values, implying the Langmuir-type adsorption between RhB molecules over the TNW-based photocatalysts. The only exceptions are found for Mn-TNW and Cu-TNW, whose $R^2$ values of the Freundlich model are higher than that of the Langmuir model, which may be due to the large error caused by the low adsorption capacity of the two catalysts. Therefore, the Langmuir model was chosen to describe the adsorption isotherms in the present work, and **Fig. 5** depicted the equilibrium adsorption characteristics of RhB of the pristine and transition-metal doped TNW photocatalysts. The equilibrium adsorption capacity ($q_e$) increases with an initial steep slope followed by slight elevation, and finally reached a plateau stage with the increase of equilibrium concentration ($C_e$). The explicit L-shape isotherms suggest that there is no strong competition between the solvent and the RhB to occupy the adsorbent active sites [55, 56].

The calculated maximum adsorption capacities ($Q_{max}$) for different samples using the Langmuir isotherm model are displayed in **Fig. 5b**. The pristine TNWs exhibit a $Q_{max}$ of 15.92 mg/g for RhB, and the introduction of transition metal elements changed the $Q_{max}$ in different ways, which are well in line with the observation in the

previous tests. The V, Cr, Ni and Zn doped TNWs present an increased $Q_{max}$ of 30-37 mg/g, while the Mn, Fe, Co and Cu doped samples show a decreased $Q_{max}$ of 4-7 mg/g. The specific surface area of the photocatalysts (yellow stars) are also plotted along the calculated $Q_{max}$ in **Fig. 5b**. The samples with high adsorption capacities, including the pristine TNW, V-TNW, Cr-TNW, Ni-TNW and Zn-TNW, generally show a higher specific surface area than the samples with low adsorption capacities, namely the Mn-TNW, Fe-TNW, Co-TNW and Cu-TNW.

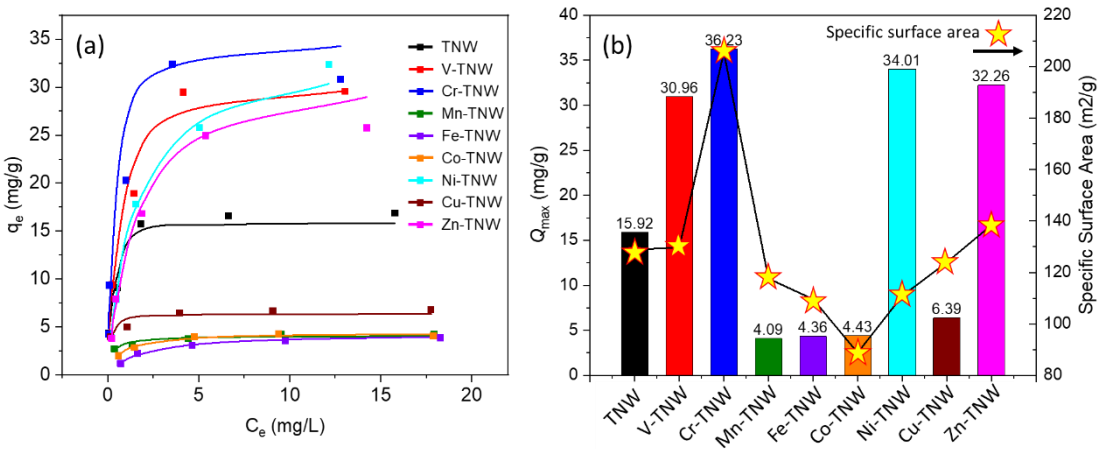


**Fig. 5.** (a) Adsorption isotherms and (b) the calculated maximum adsorption capacity ($Q_{max}$) of the pristine and transition-metal doped TNWs at 25 °C. Solid squares and lines correspond to experimental values and fitted curves obtained by Langmuir model, respectively. The specific surface area values are also presented along $Q_{max}$.

**Table 2.** Kinetic parameters for adsorption of RhB over the samples using different adsorption models.

| Kinetic models | Parameters | P25 | TNW | V-TNW | Cr-TNW | Mn-TNW | Fe-TNW | Co-TNW | Ni-TNW | Cu-TNW | Zn-TNW |
|---|---|---|---|---|---|---|---|---|---|---|---|
| Pseudo-first-order kinetic model | $k_1$ (/min) | 0.064 | 0.111 | 0.064 | 0.066 | 0.045 | 0.166 | 0.058 | 0.082 | 0.171 | 0.099 |
| | $q_{e,cal}$ (mg/g) | 1.516 | 7.916 | 18.630 | 18.620 | 3.454 | 3.452 | 5.332 | 15.660 | 2.158 | 14.520 |
| | $R^2$ | 0.743 | 0.506 | 0.835 | 0.860 | 0.376 | 0.153 | 0.470 | 0.912 | 0.245 | 0.811 |
| Pseudo-second-order kinetic model | $k_2$ (g/mg/min) | 0.049 | 0.011 | 0.004 | 0.004 | 0.008 | 0.022 | 0.007 | 0.007 | 0.057 | 0.010 |
| | $q_{e,cal}$ (mg/g) | 1.729 | 9.268 | 21.739 | 21.645 | 4.505 | 4.184 | 6.821 | 17.575 | 2.478 | 15.748 |
| | $R^2$ | 0.972 | 0.996 | 0.998 | 0.998 | 0.932 | 0.931 | 0.963 | 1.000 | 0.994 | 0.999 |
| Experimental | $q_{e,exp}$(mg/g) | 1.495 | 8.653 | 19.734 | 19.913 | 3.985 | 4.169 | 6.326 | 16.407 | 2.341 | 14.786 |
| Intra-particle diffusion model | $k_3$ | 0.285 | 1.928 | 3.480 | 3.461 | 0.746 | 0.931 | 1.121 | 3.056 | 0.591 | 3.188 |
| | $k_4$ | 0.125 | 0.336 | 1.487 | 1.610 | 0.062 | 0.108 | 0.155 | 1.436 | 0.010 | 1.037 |
| | $C_4$ | 0.505 | 4.990 | 6.421 | 5.992 | 1.850 | 2.588 | 3.025 | 5.475 | 1.848 | 7.042 |
| | $k_5$ | 0.072 | 0.364 | 0.860 | 0.832 | 0.377 | 0.235 | 0.462 | 0.477 | 0.100 | 0.344 |
| | $C_5$ | 0.844 | 4.848 | 10.607 | 10.870 | 0.141 | 1.454 | 1.098 | 11.369 | 1.333 | 11.407 |

### 3.4. Photocatalytic Activity

A photocatalytic reaction is initiated by the adsorption of photon with energy equal or greater than the bandgap of the semiconductor, generating the excited electrons ($e^-$) to the empty conduction band (CB) and the positively charged vacancy holes ($h^+$) in the valence band (VB) [1, 37]. Therefore, a proper bandgap energy is essential for the high catalytic activity of a photocatalyst. However, the wide bandgap (3.0-3.2 eV) of the pristine $TiO_2$ limits light absorption and photocatalytic efficiency. The intrinsic doping of oxygen vacancies and $Ti^{3+}$ centers as well as the extrinsic doping of transition metal elements with 3*d* electrons are efficient ways to create additional energy states below the CB of $TiO_2$ to narrow the energy bandgap [56]. The observations in the present work will show that the introduction of transition metal cations via ion-exchange can tune the bandgap of TNWs in both ways.

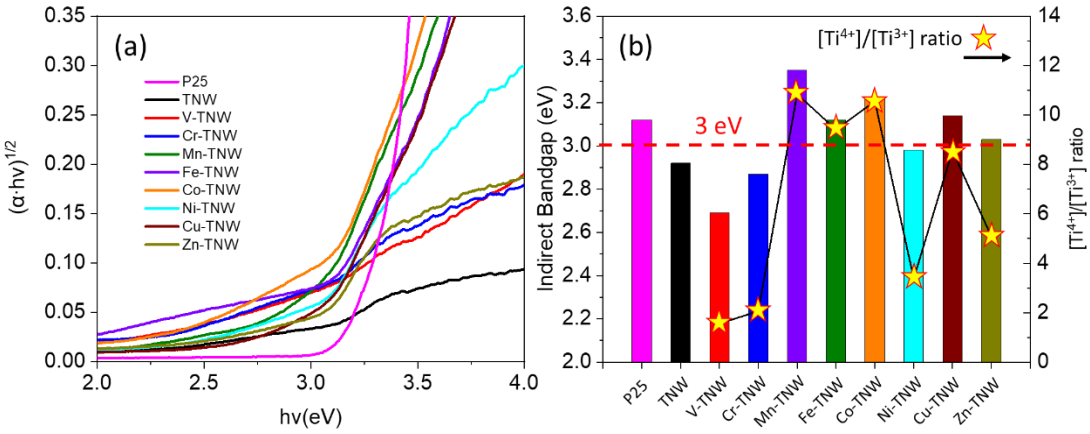


**Fig. 6.** (a) Transformed Kubelka–Munk function *vs.* the photon energy derived from the UV–vis diffuse reflectance spectra on the P25, pristine and transition-metal doped TNWs. (b) The summary of the indirect bandgap energy of the different samples along with the $[Ti^{3+}]/[Ti^{4+}]$ ratio calculated from the XPS data.

The bandgap energy of the P25, pristine and transition-metal doped TNWs are displayed in **Fig. 6** and summarized in **Table 1**. The indirect band gap energy of the pristine TNW is 2.92 eV, which is smaller than the reported value of the protonated titanate nanotubes (3.2 eV) [17]. This may suggest that the TNWs prepared by the alkali-free hydrothermal method contain high density of defects due to the amorphous nature, which creates significant intermediate energy states between the conduction and valence bands, and therefore, narrow the bandgap energy [57, 58]. The varied band gap energy helps to explain the photocatalytic activities of the TNWs doped by different transition metal elements. On the one hand, the V-TNW sample exhibits the lowest indirect bandgap energy of 2.69 eV, followed by the Cr-TNW, Ni-TNW and Zn-TNW with the bandgap energies of 2.87, 2.98 and 3.03 eV, respectively. The narrow band gap energy promotes the light adsorption efficiency, which enhances the photocatalytic activity for the degradation of RhB. On the other hand, the Mn, Fe, Co and Cu doped TNWs exhibit higher band gap energies of 3.35, 3.12, 3.22 and 3.14 eV, respectively, resulting in a limited utilization of the photon energy. Especially, the Mn-TNW sample shows the highest bandgap energy of 3.35 eV, which is quite close to the energy of the incident photon of 3.48 eV ($\lambda$ = 356 nm). Therefore, Mn-TNW showed negligible photocatalytic activity towards the degradation of RhB in **Fig. 1a**. The narrow bandgap energy alone cannot guarantee excellent photocatalytic activity, but the microstructures such as defect density, porosity and crystallinity can also influence the photocatalytic performance of the samples. As illustrated in **Fig. S5** and **Table S3** in the supporting information, the transition-metal doped anatase $TiO_2$

nanowires also exhibit low bandgap energies of 2.81-3.04 eV, indicating the efficient adsorption of UV light over these samples. However, the photocatalytic degradation results shown in **Fig. S1** reveal the poor photocatalytic activity of these samples. That is because the anatase $TiO_2$ nanowires were obtained by thermally annealing the TNWs, during which the amorphous TNWs transformed to anatase $TiO_2$ crystals, and the mesoporous networks and interlayer structures were destroyed, as shown in **Fig. S6**. With the decreased surface area and destruction of the interlayer structures, the RhB molecules cannot be sufficiently adsorbed on the surface of the photocatalysts, and therefore, the overall RhB degradation efficiency of is compromised. It's also worth noting that RhB is an organic dye that possesses sensitization properties, which may further improve the photocatalytic performance by enhancing the excitation efficiency and expanding the light absorption from UV region to visible light with lower reduction potentials in the excited states than the pristine photocatalysts [59-62]. The effects of sensitization by different organic dyes as well as the photocatalytic performance of the modified TNW and $TiO_2$ photocatalysts in the visible light region will be investigated in our future studies.

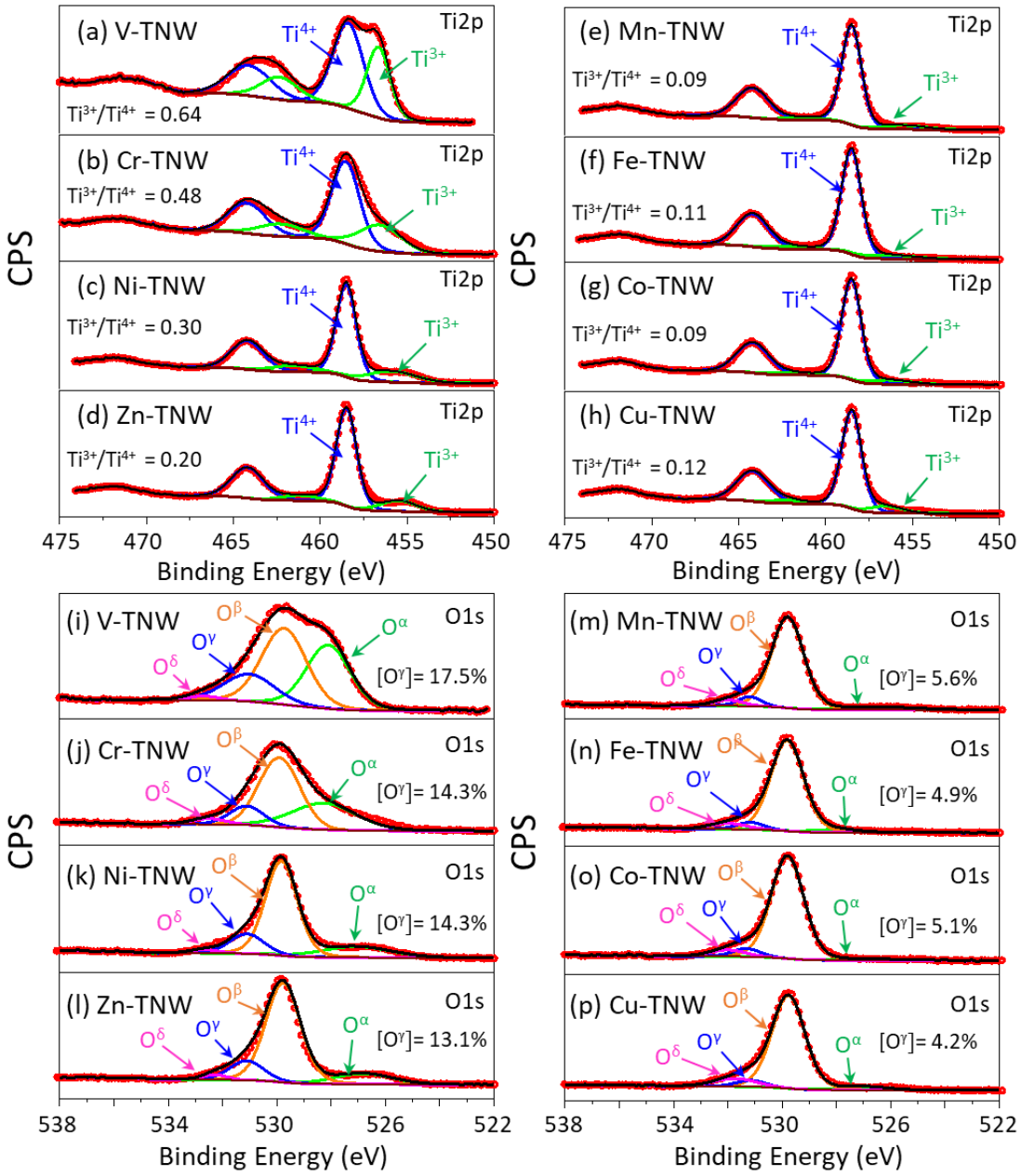


**Fig. 7.** Deconvoluted (a)-(h) Ti 2p and (i)-(p) O 1s XPS spectra of the V, Cr, Mn, Fe, Co, Ni, Cu, Zn doped TNWs along the experimental data marked in red circle. $O^{\alpha}$, $O^{\beta}$, $O^{\gamma}$ and $O^{\delta}$ represent the lattice oxygen (Ti-O-Ti), surface labile oxygen (-OH), superoxide radicals ($O_2^{\bullet -}$) and surface adsorbed water oxygen ($H_2O$), respectively.

The deconvoluted Ti 2p and O 1s XPS spectra of the transition-metal doped TNWs are displayed in **Fig. 7** and the calculated ratios of different species are summarized in

**Table 1**. The experimental data marked in **Fig. 7a-h** exhibit typical doublet features of the Ti 2p spectra, which can be deconvoluted into the $Ti^{4+}$ (Ti $2p_{3/2}$ at ~458.5 eV and $2p_{1/2}$ at ~464.2 eV) and $Ti^{3+}$ (Ti $2p_{3/2}$ at ~456 eV and $2p_{1/2}$ at ~462 eV), respectively. The deconvoluted Ti 2p spectra of pristine TNW and anatase $TiO_2$ nanowires are displayed and compared with the spectrum of V-TNW in **Fig. S7**. Although the Ti 2p spectra of TNWs (**Fig. S7a**) exhibit a typical four-peak feature, close examination of the binding energies reveals that the additional peaks result from the satellite signals rather than the $Ti^{3+}$ species, and experimental evidence support such conclusions in two ways. On the one hand, the first Ti 2p3/2 peak of the pristine TNW is located at ~458.4 eV, which corresponds to $Ti^{4+}$, rather than $Ti^{3+}$ of ~456 eV. On the other hand, the difference in binding energies (ΔBE) between the first two Ti 2p3/2 peaks of the pristine TNW is 2.7 eV, which is much larger than the ΔBE of 1.8 eV between the $Ti^{4+}$ and $Ti^{3+}$ peaks of the V-TNW sample shown in **Fig. S7c**. Therefore, the additional Ti 2p3/2 peak at 461.7 eV is assigned to the satellite peak, which agrees with the reports by Oku *et. al.* [63] and our previous observations [30]. Moreover, the valence states of the Ti ions were further examined by the electron energy loss spectroscopy (EELS) with the $L_{3,2}$ energy loss near edge fine structure (ELNES) of titanium over the selected samples displayed and compared in **Fig. 8**. As shown, the EELS spectra of the Ti $L_{2,3}$-edge for the pristine TNW and Mn-TNW exhibit distinct four-peak feature, indicating that the $Ti^{4+}$ species dominate the surface of the catalysts. The Ti $L_{2,3}$-edge of the Cu-TNW sample shows a broadened doublet-peak feature (**Fig. 8c**), which reveals the increase in the surface $Ti^{3+}$ ratio. For the Cr-TNW (**Fig. 8d**) and V-TNW

(**Fig. 8e**) catalysts, no splitting of the $L_2$ and $L_3$ peaks into a doublet is resolved, indicating a domination of $Ti^{3+}$ at the surface region [64]. The evolution in the Ti $L_{2,3}$-edge spectra of the selected samples agree well with the change in the $[Ti^{3+}]/[Ti^{4+}]$ ratio determined by the XPS analysis, as marked in **Fig. 8**. The confirmed exclusion of $Ti^{3+}$ in the pristine TNWs indicate that the $Ti^{3+}$ species in the transition-metal doped TNWs result from partial reduction of $Ti^{4+}$ in the TNW lattice. Liu *et. al.* [6] reported that the introduction of La can substitute the surface Ti atom of the $TiO_2$, which leads to the generation of oxygen vacancies and $Ti^{3+}$ for charge balance. Therefore, the doping of transition metal cations of $V^{5+}$, $Cr^{3+}$, $Ni^{2+}$ and $Zn^{2+}$ also results in the partial reduction of $Ti^{4+}$ to $Ti^{3+}$ to promote the photocatalytic reactivity.

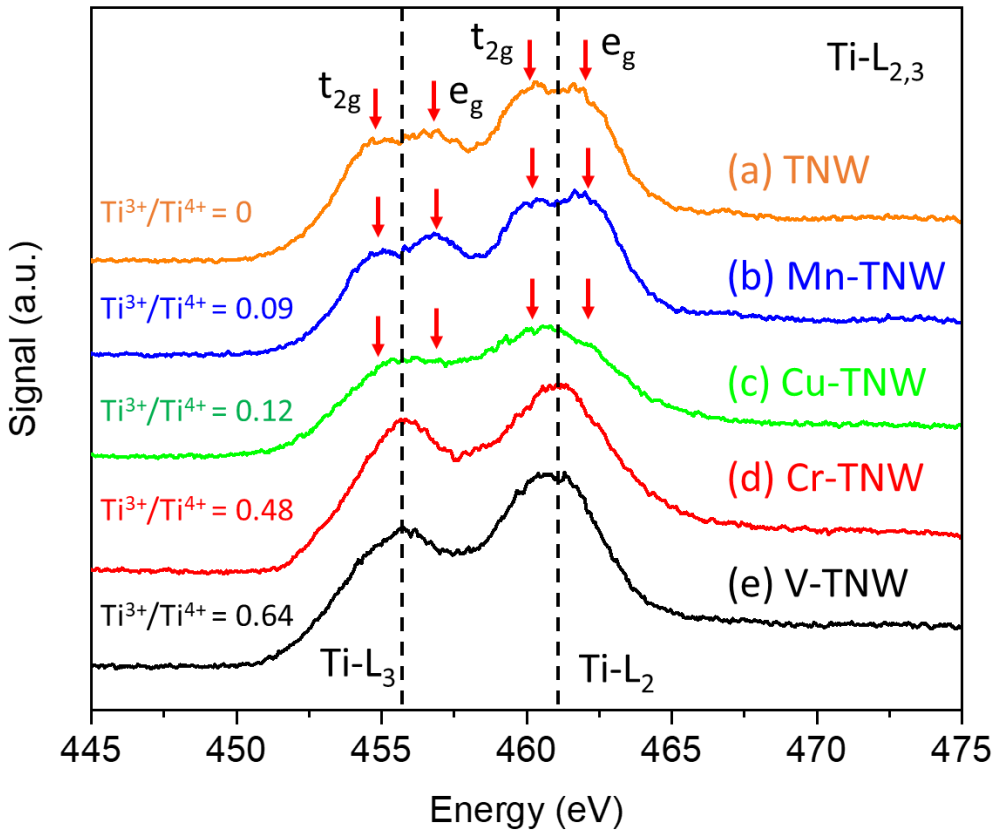


**Fig. 8.** The EELS spectra of the Ti $L_{2,3}$-edge for the (a) pristine TNW, (b) Mn-TNW, (c) Cu-TNW, (d) Cr-TNW and (e) V-TNW.

The $Ti^{4+}$ and $Ti^{3+}$ contents on the surface of the samples were calculated according to the deconvoluted peak areas. As displayed in **Table 1**, the V-TNW, Cr-TNW, Ni-TNW and Zn-TNW samples exhibit high surface $Ti^{3+}$ concentrations of 39, 32.6, 22.8, 16.4 at.%, respectively, which are higher than the Mn, Fe, Co and Cu doped samples of 8.4, 9.6, 8.7 and 10.5 at.%, respectively. The calculated surface $Ti^{3+}$ concentrations using the XPS data are highly in line with the bandgap energy obtained from the UV-vis spectroscopy. As illustrated in **Fig. 6b**, the samples with higher $[Ti^{3+}]/[Ti^{4+}]$ ratios exhibit lower bandgap energy, resulting from the additional energy states generated by the $Ti^{3+}$ centers below the CB.

The deconvoluted O 1s spectra of the pristine and the transition-metal doped TNWs are displayed in **Fig. S8** and **Fig. 7i-p**, respectively, which can be assigned to four oxygen species [65, 66]: (i) lattice oxygen from Ti–O in the $TiO_2$ crystal lattice (526.5–528.3 eV, $O^{\alpha}$), (ii) surface labile oxygen from the Ti–OH groups (529.7–529.9 eV, $O^{\beta}$), (iii) superoxide radicals $O_2^{\bullet -}$ (531.1 eV, $O^{\gamma}$), and (iv) surface adsorbed molecular water (above 532 eV, $O^{\delta}$). The ratios of different species are calculated according to the deconvoluted peak areas, as summarized in **Table 1**. The most important oxygen species for photocatalytic degradation of RhB is the superoxide radical ($O^{\gamma}$). She *et. al.* [65] reported that the superoxide radical groups can serve as the electron carriers, which facilitate the separation of the electron-hole pairs, and therefore enhance the photocatalytic performance of the $TiO_2$ photocatalysts. In the present work, based on the deconvoluted XPS spectra, the concentration of the superoxide radicals varied according to the transition metal dopants. The pristine

TNWs exhibit the highest superoxide radical ratio of 26.5% (**Fig. S8**), and the V, Cr, Ni and Zn doped TNWs show higher concentrations of superoxide radicals of 13.0-17.5% than the Mn, Fe, Co and Cu doped samples of 4.2-5.6%.

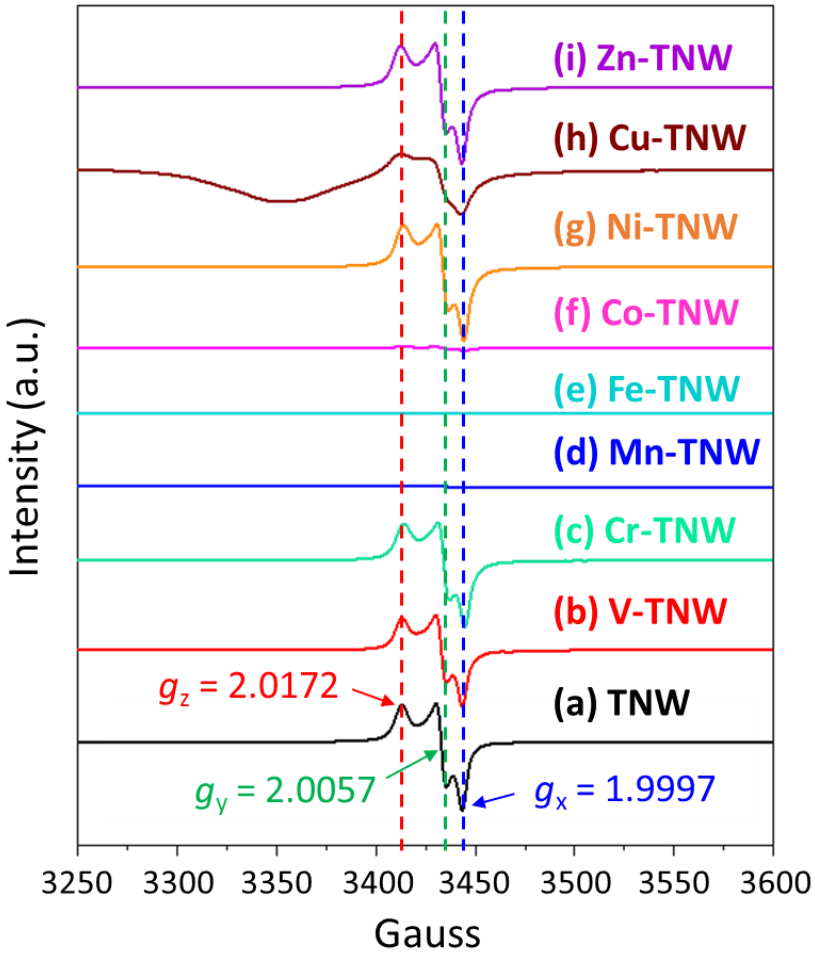


**Fig. 9.** The EPR spectra of the pristine and transition-metal doped TNWs.

The presence of abundant superoxide radical groups on the V-TNW, Cr-TNW, Ni-TNW and Zn-TNW samples was also supported by the electron paramagnetic resonance (EPR) spectra displayed in **Fig. 9**. The pristine TNW, V-TNW, Cr-TNW, Ni-TNW and Zn-TNW exhibit doublet resonance with anisotropic *g*-tensors of $g_x$ = 1.9997, $g_y$ = 2.0057, $g_z$ = 2.0172, indicating the existence of the superoxide radical centers on the surface of these photocatalysts [12, 67]. Especially, Carter *et. al.* [68]

reported superoxide radicals ($O_2^{\bullet-}$) stabilized at the surface oxygen vacancies on the thermally reduced P25 $TiO_2$ polycrystalline, which are featured with similar doublet resonance envelopes and *g*-tensors as well as the observation over the pristine and the V, Cr, Ni and Zn doped TNWs. The superoxide radicals ($O_2^{\bullet-}$) can be produced by the $O_2$ molecules adsorbed on the surface of $TiO_2$ activated by the photo-induced electrons and the free electrons located on the oxygen vacancies [11]. The superoxide radical groups are strong oxidizing agents which can facilitate the charge carrier separation and promote the oxidation of organic substances [69]. Moreover, the $O_2$ does not adsorb on a perfect neutral $TiO_2$ surface but requires excess negative charge to form the O-Ti bonds, which can be provided by subsurface oxygen vacancies. Therefore, the strong EPR resonance also reflects the abundant oxygen vacancy defects over the V, Cr, Ni and Zn doped samples. The silent EPR signals from the Mn, Fe and Co doped samples can be ascribed to the annihilation of defects in the materials due to the increased crystallinity. The Cu-TNW samples showed weak EPR signals, which agrees with the relatively lower crystallinity (93%) than the Mn, Fe and Co doped samples (96-99%). Moreover, detailed comparison of the photocatalytic degradation performance of the transition-metal doped TNWs in **Fig. 1a** shows the better photocatalytic activity of the Cu-TNW than the other three samples with high crystallinity. Meanwhile, the EPR spectra of the TNW and anatase $TiO_2$ nanowires as well as the commercial P25 powders are compared in **Fig. S9**. The diminished EPR signals of the anatase $TiO_2$ nanomaterials indicated the extinction of the superoxide radicals during the thermal annealing, which helps to explain the compromised

photocatalytic activity for RhB degradation of the anatase based photocatalysts in **Fig. S1**. Therefore, the observations above demonstrate that the defective structures are important to the TNW-based photocatalysts, which not only helps to narrow the bandgap to enhance the light adsorption ability, but also generates abundant superoxide radical species to facilitate the photocatalyst reactions. It should also be noted that the abundant surface superoxide radicals alone cannot guarantee a high overall RhB removal efficiency of the photocatalyst [70, 71]. For example, the pristine TNW with the highest superoxide radical ratio of 26.5% exhibited a lower performance than the V, Cr, Ni and Zn doped TNWs with a relatively lower $O_2^{\bullet-}$ concentrations of 13.0-17.5%. That is partially because the pristine TNWs lack the large mesopores of 5-20 nm brought by the ion-exchange process, which plays important roles in developing the advanced porosity networks with the inherit mesopores of 3-4.5 nm. Therefore, the effects of transition metal ion-exchange are complicated, and the multiple synergies result in the improved adsorption properties and photocatalytic performance of the V, Cr, Ni and Zn doped TNWs.

### 3.5. Catalyst Stability

Finally, the photocatalytic stability of the pristine and the V, Cr, Ni and Zn doped TNWs were evaluated through simultaneous adsorption and photocatalytic degradation of RhB under UV irradiation continuously for 5 cycles. As presented in **Fig. 10**, the initial concentration of RhB was 5 mg/L, and RhB was replenished at the end of each cycle (every 60 min) to keep the nominal concentration at 5 mg/L. Detailed stability testing procedures are presented in **Table S1** in the supporting

information. In line with the sequential adsorption and photocatalytic degradation results are shown in **Fig. 1**, the transition-metal doped photocatalysts showed an enhanced removal efficiency of RhB compared to the pristine TNWs in Cycle 1. In the subsequent testing cycles, however, the residue RhB concentration in the V-TNW catalyzed suspension kept increasing, indicating the decreased RhB removal efficiency and the poor photocatalytic stability of the V-TNW photocatalysts. For the other samples, although an increase in the residue RhB concentration was also observed, high RhB removal efficiency can be maintained after 5 continuous testing cycles. The RhB concentration profiles of the Cr-TNW, Ni-TNW and Zn-TNW did not reach the plateau limits at the end of the $4^{th}$ and $5^{th}$ cycles, suggesting that higher RhB degradation efficiency can be achieved with extended irradiation time. The decreased RhB removal efficiency of the photocatalyst may result from the saturated adsorption of the dye molecules over the active sites of the photocatalysts, which can be supported by the deepening pink color of the catalyst powders along the testing cycles. As demonstrated in the adsorption kinetic studies, the diffusion of RhB molecules in the TNW based photocatalysts is controlled by the intra-particle diffusion, and the RhB removal efficiency of these samples strongly depends on the mesopores of 3-4.5 nm. Therefore, the RhB molecules adsorbed and saturated on the active sites on the mesoporous TNW-based photocatalysts during the extended testing cycles, which not only slows down the intra-particle diffusion, but also compromised the light utilization efficiency of the photocatalysts. Therefore, a longer irradiation time is needed to achieve the complete degradation of the RhB in the solution.

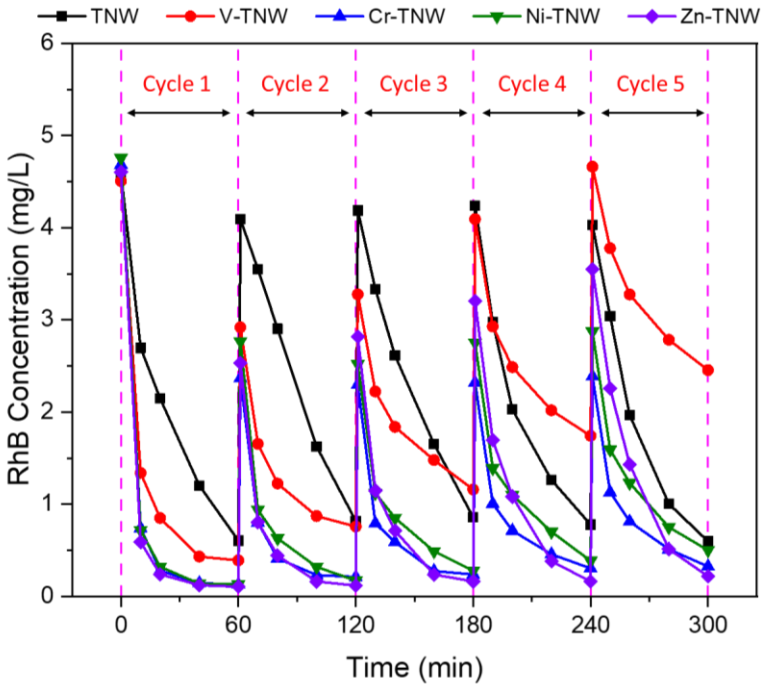


**Fig. 10.** Stability tests of the pristine and V, Cr, Ni and Zn doped TNW photocatalysts for simultaneous adsorption and photocatalytic degradation of RhB for 5 cycles. RhB was replenished every 60 min to keep the nominal RhB concentration at 5 mg/L.

The FTIR spectra of the transition metal ion-exchanged TNW samples before and after the RhB adsorption and photocatalytic degradation tests are summarized and displayed in **Fig. 11a** and **b**, respectively. The strong absorption band centered at 490 $cm^{-1}$ can be assigned to the Ti–O–Ti stretching vibration [72, 73], and the presence of a binding vibration of $H_2O$ (or $H_3O^+$) at 1620 $cm^{-1}$ and a broad vibration band of O-H groups at 2500-3500 $cm^{-1}$ demonstrate the existence of large amounts of water and hydroxy groups in all the TNW-based photocatalysts [74-77]. Meanwhile, close scrutiny of **Fig. 11a** reveals the presence of an absorption band centered at 905 $cm^{-1}$ in the FTIR spectra of the pristine TNW and the V, Cr, Ni and Zn ion-exchanged samples. The absorption band can be assigned to the symmetric Ti–$O_2$ stretching

vibration [67], indicating the existence of superoxide radicals in these samples, which agrees with the results of XPS. Furthermore, new vibration bands emerged at 1150-1200 and 2800-2950 $cm^{-1}$ in the samples after the RhB adsorption and photocatalytic degradation tests, which can be assigned to the C-H and C-O stretching modes originated from the residue RhB at the surface of the photocatalysts [78-83]. Especially, the intensities of these vibration bands are stronger in the spectra of the Mn, Fe, Co and Cu ion-exchanged sample than the other samples, which may result from the higher amount of residue RhB due to the lower photocatalytic activity over these samples.

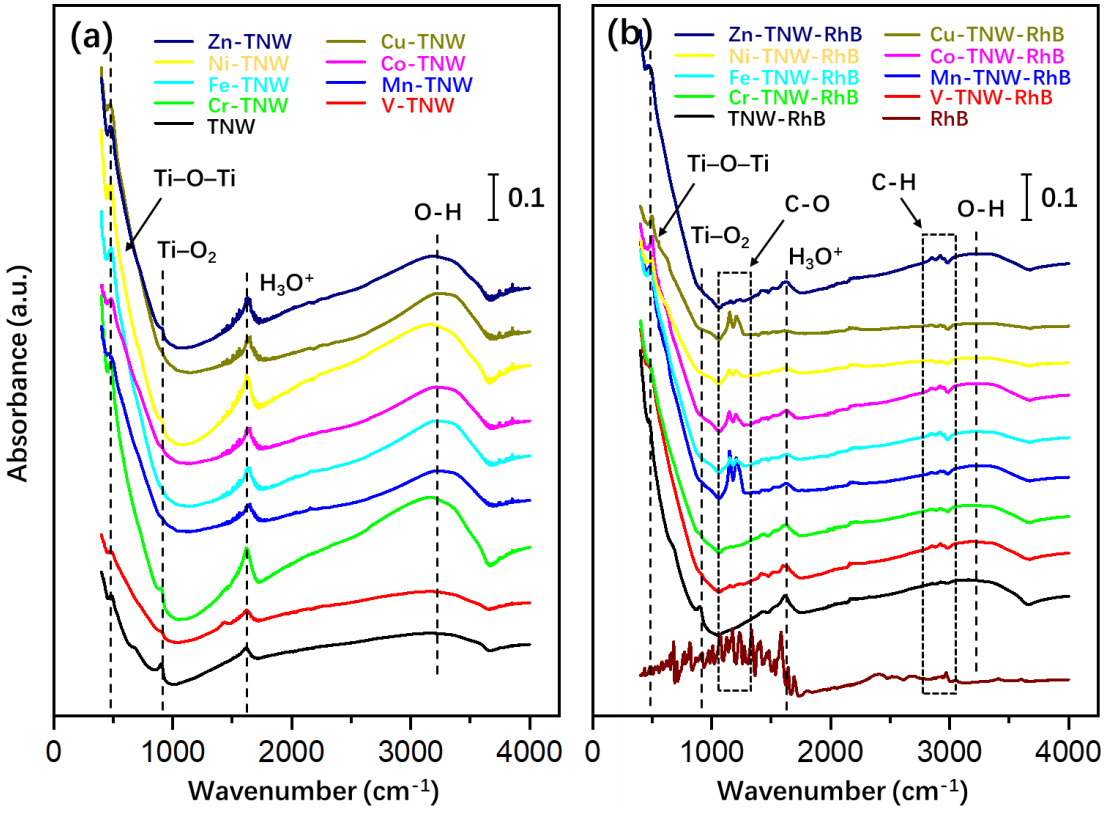


**Fig. 11.** FTIR spectra of the pristine and transition metal ion-exchanged TNWs (a) before and (b) after the RhB adsorption and photocatalytic degradation tests.

## 4. Ion-Exchange Assisted Microstructure Engineering

Based on the photocatalytic activity evaluation, adsorption kinetics, and material characterization, the enhanced removal efficiency of RhB by the transition-metal (V, Cr, Ni and Zn) doped TNWs can be elucidated as follows, and the proposed mechanisms of microstructure engineering of TNWs by the ion-exchange assisted transition-metal doping are illustrated in **Fig. 12**.

1) The pristine TNWs prepared by the alkali-free hydrothermal method are of poor crystallinity with abundant ion-exchangeable sites, surface defects and superoxide radicals, as well as high surface area with small mesopores of ~3.6-4.5 nm.
2) Upon the introduction of transition metal elements via ion-exchange, large mesopores of 5-20 nm are generated, which facilitate the mass transfer of the dye molecules from the bulk solution into the catalyst. Meanwhile, the V, Cr, Ni and Zn doped TNWs also maintain the original small mesopores of ~3.6-4.5 nm and active sites, resulting in the enhanced overall adsorption capacity of the catalysts.
3) Besides the modifications in the microstructures, the V, Cr, Ni and Zn dopant atoms also substitute for the surface Ti atoms in the TNW framework and generate oxygen vacancies and $Ti^{3+}$ for charge balance. The intrinsic oxygen vacancies and $Ti^{3+}$ centers together with the extrinsic transition metal atoms with 3*d* electrons generate the additional energy states below the CB, which narrows the energy bandgap and enhances the light utilization efficiency.
4) By combining the well-developed porosity networks, high surface area, abundant surface superoxide radicals, and improved light absorption with reduced energy

bandgap, the V, Cr, Ni and Zn doped TNWs catalysts exhibit excellent photocatalytic efficiency to remove RhB from aqueous solutions.

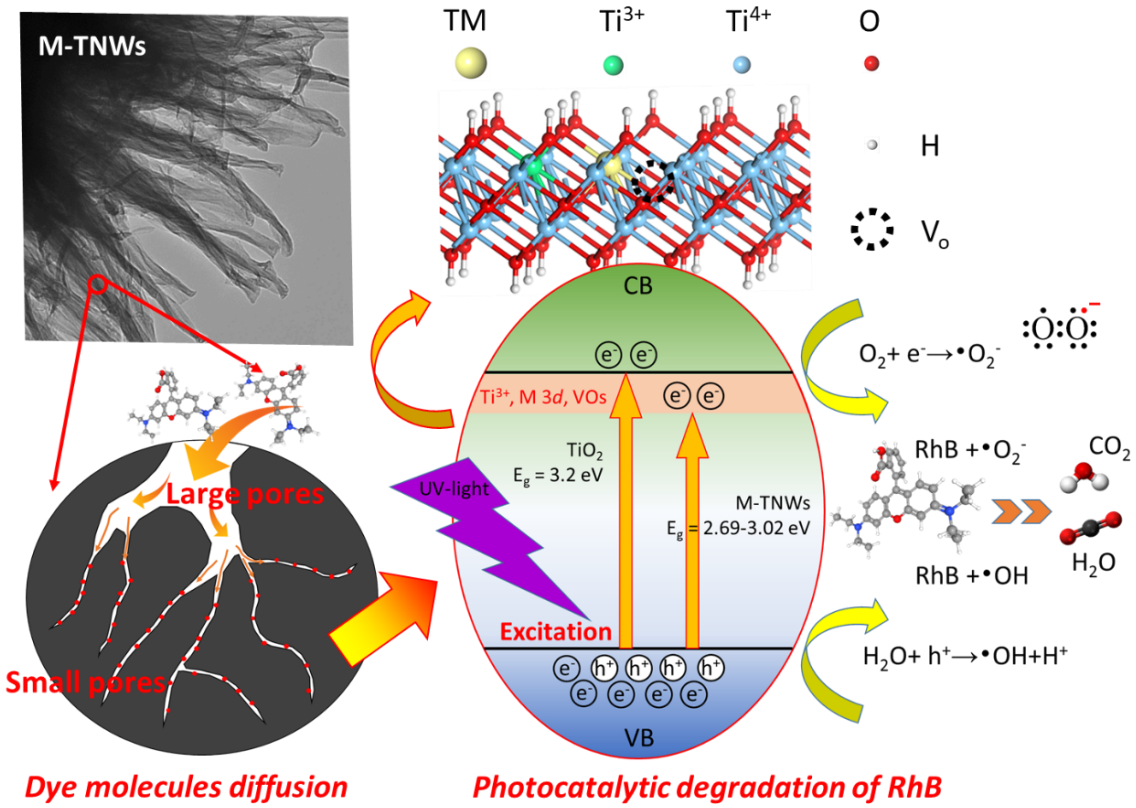


**Fig. 12.** Schematic illustration of the proposed reaction mechanisms of the photocatalytic degradation of RhB by the transition-metal doped TNW photocatalysts.

## 5. Conclusion

In summary, a series of transition-metal doped titanate nanowires were prepared via a facile ion-exchange process over pristine protonated titanate nanostructures and were evaluated for the degradation of RhB in aqueous solutions under UV irradiation. Based on the RhB removal efficiencies, the eight dopant elements tested are categorized into three groups: i) V, Cr, Ni and Zn with enhanced adsorption capacity and excellent photocatalytic activity; ii) Fe, Co and Cu with decreased adsorption

capacity but moderate photocatalytic activity; and iii) Mn with negligible adsorption capacity and poor photocatalytic activity. The varied RhB removal efficiencies result from the microstructure modifications associated with the changes of porosity and electronic properties due to the transition-metal intercalations in the TNW matrix. The enhanced RhB adsorption capacity of the V, Cr, Ni and Zn doped catalysts are attributed to the newly developed large mesopores of ~5-20 nm while inheriting the small mesopores of ~3.6-4.5 nm from the pristine TNWs. The combination of the large and small mesopores enables the efficient mass transfer and the high surface area, which are absent in the Mn, Fe, Co and Cu doped catalysts due to the large-size ion intercalation induced destruction of the layered structures and mesopores. Meanwhile, the incorporation of V, Cr, Ni and Zn cations results in the reduction of $Ti^{4+}$ to $Ti^{3+}$ ions in the TNW matrix. The newly formed $Ti^{3+}$ centers together with the oxygen vacancies and superoxide radicals from the pristine TNWs help to narrow the optical bandgaps, improve the light adsorption, and enhance the photocatalytic reactivity of the transition-metal doped TNW photocatalysts. Therefore, the present work sheds light on the development of highly efficient titanate-based photocatalysts through rational microstructure engineering for the wastewater treatment.

## CReDit Authorship Contribution Statement

**Xingxu Lu:** Data curation, Formal analysis, Investigation, Methodology, Software, Validation, Visualization, Writing - original draft, Writing - review & editing. **Fangyuan Liu:** Investigation, Methodology, Data curation. **Yanliu Dang:** Investigation, Methodology, Data curation. **Meilin Li:** Investigation, Methodology,

Data curation. **Mingyue Ruan:** Investigation, Methodology. **Mudi Wu:** Investigation. **Chunxiang Zhu:** Investigation, Methodology. **Tomoyasu Mani:** Investigation, Methodology. **Steven L. Suib:** Resources, Supervision. **Pu-Xian Gao:** Funding acquisition, Project administration, Supervision, Investigation, Validation, Writing - review & editing

## Declaration of Competing Interest

The authors declare that they have no known competing financial interests or personal relationships that could have appeared to influence the work reported in this paper.

## Acknowledgements

The authors thank the financial support from the US Department of Energy (Award Nos. DE-SC0018890 and DE-EE0008423), the US National Science Foundation (Award No. IIP 1919231), and the University of Connecticut IMMP and CARIC programs. The electron microscopy studies were performed using the facilities in the UConn/ThermoFisher Scientific Center for Advanced Microscopy and Materials Analysis (CAMMA). Xingxu Lu is grateful to Prof. Clyde Cady and Ms. Wen Zhao from Department of Chemistry of UConn for their insightful discussion on the EPR spectroscopy.

## Reference

[1] J. Schneider, M. Matsuoka, M. Takeuchi, J. Zhang, Y. Horiuchi, M. Anpo, D.W. Bahnemann, Understanding $TiO_2$ Photocatalysis: Mechanisms and Materials, Chem. Rev., 114 (2014) 9919-9986, https://doi.org/10.1021/cr5001892.

[2] S. Hoang, Y. Guo, A.J. Binder, W. Tang, S. Wang, J. Liu, H. Tran, X. Lu, Y. Wang, Y. Ding, E.A. Kyriakidou, J. Yang, T.J. Toops, T.R. Pauly, R. Ramprasad, P.-X. Gao, Activating low-temperature diesel oxidation by single-atom Pt on $TiO_2$ nanowire array, Nat. Commun., 11 (2020) 1062, https://doi.org/10.1038/s41467-020-14816-w.

[3] X. Lu, M. Li, S. Hoang, S.L. Suib, P.-X. Gao, Solvent effects on the heterogeneous growth of $TiO_2$ nanostructure arrays by solvothermal synthesis, Catal. Today, 360 (2021) 275-283, https://doi.org/10.1016/j.cattod.2020.02.044.

[4] N. Liu, X. Zhou, N.T. Nguyen, K. Peters, F. Zoller, I. Hwang, C. Schneider, M.E. Miehlich, D. Freitag, K. Meyer, D. Fattakhova-Rohlfing, P. Schmuki, Black Magic in Gray Titania: Noble-Metal-Free Photocatalytic $H_2$ Evolution from Hydrogenated Anatase, ChemSusChem, 10 (2017) 62-67, https://doi.org/10.1002/cssc.201601264.

[5] S. Mohajernia, P. Andryskova, G. Zoppellaro, S. Hejazi, S. Kment, R. Zboril, J. Schmidt, P. Schmuki, Influence of $Ti^{3+}$ defect-type on heterogeneous photocatalytic $H_2$ evolution activity of $TiO_2$, J. Mater. Chem. A, 8 (2020) 1432-1442, https://doi.org/10.1039/C9TA10855F.

[6] Y. Liu, S. Zhou, J. Li, Y. Wang, G. Jiang, Z. Zhao, B. Liu, X. Gong, A. Duan, J. Liu, Y. Wei, L. Zhang, Photocatalytic reduction of $CO_2$ with water vapor on surface La-modified $TiO_2$ nanoparticles with enhanced $CH_4$ selectivity, Appl. Catal. B, 168-169 (2015) 125-131, https://doi.org/10.1016/j.apcatb.2014.12.011.

[7] J. Low, S. Qiu, D. Xu, C. Jiang, B. Cheng, Direct evidence and enhancement of surface plasmon resonance effect on Ag-loaded $TiO_2$ nanotube arrays for photocatalytic $CO_2$ reduction, Appl. Surf. Sci., 434 (2018) 423-432,

https://doi.org/10.1016/j.apsusc.2017.10.194.

[8] L. Yao, J. He, T. Li, T. Ren, Novel $SiO_2/H_2Ti_2O_5.H_2O$-Nanochain Composite with High UV-Visible Photocatalytic Activity for Supertransparent Multifunctional Thin Films, Langmuir, 32 (2016) 13611-13619, https://doi.org/10.1021/acs.langmuir.6b03532.

[9] L. Wen, R. Xu, C. Cui, W. Tang, Y. Mi, X. Lu, Z. Zeng, S.L. Suib, P.-X. Gao, Y. Lei, Template-Guided Programmable Janus Heteronanostructure Arrays for Efficient Plasmonic Photocatalysis, Nano Lett., 18 (2018) 4914-4921, https://doi.org/10.1021/acs.nanolett.8b01675.

[10] Y. Chen, M. Xu, J. Wen, Y. Wan, Q. Zhao, X. Cao, Y. Ding, Z.L. Wang, H. Li, Z. Bian, Selective recovery of precious metals through photocatalysis, Nat. Sustain., (2021), https://doi.org/10.1038/s41893-021-00697-4.

[11] X. Pan, M.-Q. Yang, X. Fu, N. Zhang, Y.-J. Xu, Defective $TiO_2$ with oxygen vacancies: synthesis, properties and photocatalytic applications, Nanoscale, 5 (2013) 3601-3614, https://doi.org/10.1039/C3NR00476G.

[12] A. Naldoni, M. Altomare, G. Zoppellaro, N. Liu, Š. Kment, R. Zbořil, P. Schmuki, Photocatalysis with Reduced $TiO_2$: From Black $TiO_2$ to Cocatalyst-Free Hydrogen Production, ACS Catal., 9 (2019) 345-364, https://doi.org/10.1021/acscatal.8b04068.

[13] Q. Wu, R. van de Krol, Selective Photoreduction of Nitric Oxide to Nitrogen by Nanostructured $TiO_2$ Photocatalysts: Role of Oxygen Vacancies and Iron Dopant, J. Am. Chem. Soc., 134 (2012) 9369-9375, https://doi.org/10.1021/ja302246b.

[14] Q. Wu, Q. Zheng, R. van de Krol, Creating Oxygen Vacancies as a Novel

Strategy To Form Tetrahedrally Coordinated $Ti^{4+}$ in Fe/$TiO_2$ Nanoparticles, J. Phys. Chem. C, 116 (2012) 7219-7226, https://doi.org/10.1021/jp212577g.

[15] J. Low, B. Cheng, J. Yu, Surface modification and enhanced photocatalytic $CO_2$ reduction performance of $TiO_2$: a review, Appl. Surf. Sci., 392 (2017) 658-686, https://doi.org/10.1016/j.apsusc.2016.09.093.

[16] K. Kordás, M. Mohl, Z. Kónya, Á. Kukovecz, Layered titanate nanostructures: perspectives for industrial exploitation, Transl. Mater. Res., 2 (2015) 015003, https://doi.org/10.1088/2053-1613/2/1/015003.

[17] Á. Kukovecz, K. Kordás, J. Kiss, Z. Kónya, Atomic scale characterization and surface chemistry of metal modified titanate nanotubes and nanowires, Surf. Sci. Rep., 71 (2016) 473-546, https://doi.org/10.1016/j.surfrep.2016.06.001.

[18] X. Lu, W. Tang, S. Du, L. Wen, J. Weng, Y. Ding, W.S. Willis, S.L. Suib, P.-X. Gao, Ion-Exchange Loading Promoted Stability of Platinum Catalysts Supported on Layered Protonated Titanate-Derived Titania Nanoarrays, ACS Appl. Mater. Interfaces, 11 (2019) 21515-21525, https://doi.org/10.1021/acsami.9b04378.

[19] N. Sutradhar, A. Sinhamahapatra, S.K. Pahari, H.C. Bajaj, A.B. Panda, Room temperature synthesis of protonated layered titanate sheets using peroxo titanium carbonate complex solution, ChemComm, 47 (2011) 7731-7733, https://doi.org/10.1039/c1cc12116b.

[20] X. Lu, W. Tang, P.-X. Gao, Nanostructured $TiO_2$ Support Effect on Hydrothermal Stability of Platinum based Catalysts, Microsc. Microanal., 24 (2018) 1642-1643, https://doi.org/10.1017/S1431927618008693.

[21] V. Kumaravel, S. Mathew, J. Bartlett, S.C. Pillai, Photocatalytic hydrogen production using metal doped $TiO_2$: A review of recent advances, Appl. Catal. B, 244 (2019) 1021-1064, https://doi.org/10.1016/j.apcatb.2018.11.080.

[22] C. Zou, X. Zhao, Y. Xu, One-dimensional zirconium-doped titanate nanostructures for rapid and capacitive removal of multiple heavy metal ions from water, Dalton Trans., 47 (2018) 4909-4915, https://doi.org/10.1039/C8DT00405F.

[23] M. Nawaz, W. Miran, J. Jang, D.S. Lee, One-step hydrothermal synthesis of porous 3D reduced graphene oxide/$TiO_2$ aerogel for carbamazepine photodegradation in aqueous solution, Appl. Catal. B, 203 (2017) 85-95, https://doi.org/10.1016/j.apcatb.2016.10.007.

[24] D. Dodoo-Arhin, T. Asiedu, B. Agyei-Tuffour, E. Nyankson, D. Obada, J.M. Mwabora, Photocatalytic degradation of Rhodamine dyes using zinc oxide nanoparticles, Mater. Today: Proc., 38 (2021) 809-815, https://doi.org/10.1016/j.matpr.2020.04.597.

[25] L. Xiong, W. Sun, Y. Yang, C. Chen, J. Ni, Heterogeneous photocatalysis of methylene blue over titanate nanotubes: Effect of adsorption, J. Colloid Interface Sci., 356 (2011) 211-216, https://doi.org/10.1016/j.jcis.2010.12.059.

[26] Y. Ide, Y. Nakasato, M. Ogawa, Molecular Recognitive Photocatalysis Driven by the Selective Adsorption on Layered Titanates, J. Am. Chem. Soc., 132 (2010) 3601-3604, https://doi.org/10.1021/ja910591v.

[27] A. Sandoval, C. Hernández-Ventura, T.E. Klimova, Titanate nanotubes for removal of methylene blue dye by combined adsorption and photocatalysis, Fuel, 198

(2017) 22-30, https://doi.org/10.1016/j.fuel.2016.11.007.

[28] C.H. Nguyen, R.-S. Juang, Efficient removal of methylene blue dye by a hybrid adsorption–photocatalysis process using reduced graphene oxide/titanate nanotube composites for water reuse, J. Ind. Eng. Chem., 76 (2019) 296-309, https://doi.org/10.1016/j.jiec.2019.03.054.

[29] Y. Lin, J. Ma, W. Liu, Z. Li, K. He, Efficient removal of dyes from dyeing wastewater by powder activated charcoal/titanate nanotube nanocomposites: adsorption and photoregeneration, Environ. Sci. Pollut. Res., 26 (2019) 10263-10273, https://doi.org/10.1007/s11356-019-04218-x.

[30] X. Lu, S. Hoang, W. Tang, S. Du, S. Wang, F. Liu, W. Zhong, S.L. Suib, G. Yang, F.-Y. Zhang, P.-X. Gao, Direct Synthesis of Conformal Layered Protonated Titanate Nanoarray Coatings on Various Substrate Surfaces Boosted by Low-Temperature Microwave-Assisted Hydrothermal Synthesis, ACS Appl. Mater. Interfaces, 10 (2018) 35164-35174, https://doi.org/10.1021/acsami.8b11801.

[31] C. Guo, L. Xu, J. He, L. Hu, B. Wang, L. Da, Enhanced Photocatalytic Activity by $Cu_2O$ Nanoparticles Integrated $H_2Ti_3O_7$ Nanotubes for Removal of Mercaptan, Nano, 12 (2017) 1750075, https://doi.org/10.1142/S1793292017500758.

[32] X. Lu, W. Tang, M. Li, Y. Dang, N. Campbell, Z. Li, S.L. Suib, P.-X. Gao, Mass transport in nanoarray monolithic catalysts: An experimental-theory study, Chem. Eng. J., 405 (2021) 126906, https://doi.org/10.1016/j.cej.2020.126906.

[33] S. Hoang, X. Lu, W. Tang, S. Wang, S. Du, C.-Y. Nam, Y. Ding, R.D. Vinluan, J. Zheng, P.-X. Gao, High performance diesel oxidation catalysts using ultra-low Pt

loading on titania nanowire array integrated cordierite honeycombs, Catal. Today, 320 (2019) 2-10, https://doi.org/10.1016/j.cattod.2017.11.019.

[34] T. Boningari, D.K. Pappas, P.G. Smirniotis, Metal oxide-confined interweaved titania nanotubes M/TNT (M = Mn, Cu, Ce, Fe, V, Cr, and Co) for the selective catalytic reduction of $NO_x$ in the presence of excess oxygen, J. Catal., 365 (2018) 320-333, https://doi.org/10.1016/j.jcat.2018.07.010.

[35] W. Tang, X. Lu, F. Liu, S. Du, J. Weng, S. Hoang, S. Wang, C.-Y. Nam, P.-X. Gao, Ceria-based nanoflake arrays integrated on 3D cordierite honeycombs for efficient low-temperature diesel oxidation catalyst, Appl. Catal. B, 245 (2019) 623-634, https://doi.org/10.1016/j.apcatb.2019.01.028.

[36] W. Tang, X. Lu, J. Weng, P.-X. Gao, NiO nanosheet array integrated monoliths for low temperature catalytic propane oxidation: A study on the promotion effect of Ce doping, Catal. Today, 360 (2021) 194-203, https://doi.org/10.1016/j.cattod.2020.07.086.

[37] N. Tian, K. Xiao, Y. Zhang, X. Lu, L. Ye, P. Gao, T. Ma, H. Huang, Reactive sites rich porous tubular yolk-shell g-$C_3N_4$ via precursor recrystallization mediated microstructure engineering for photoreduction, Appl. Catal. B, 253 (2019) 196-205, https://doi.org/10.1016/j.apcatb.2019.04.036.

[38] R. Acosta-Herazo, M.Á. Mueses, G.L. Puma, F. Machuca-Martínez, Impact of photocatalyst optical properties on the efficiency of solar photocatalytic reactors rationalized by the concepts of initial rate of photon absorption (IRPA) dimensionless boundary layer of photon absorption and apparent optical thickness, Chem. Eng. J.,

356 (2019) 839-849, https://doi.org/10.1016/j.cej.2018.09.085.

[39] J. Diaz-Angulo, I. Gomez-Bonilla, C. Jimenez-Tohapanta, M. Mueses, M. Pinzon, F. Machuca-Martinez, Visible-light activation of $TiO_2$ by dye-sensitization for degradation of pharmaceutical compounds, Photochem. Photobiol. Sci., 18 (2019) 897-904, https://doi.org/10.1039/C8PP00270C.

[40] A. Tolosana-Moranchel, C. Pecharromán, M. Faraldos, A. Bahamonde, Strong effect of light scattering by distribution of $TiO_2$ particle aggregates on photocatalytic efficiency in aqueous suspensions, Chem. Eng. J., 403 (2021) 126186, https://doi.org/10.1016/j.cej.2020.126186.

[41] W. Gao, J. Lu, S. Zhang, X. Zhang, Z. Wang, W. Qin, J. Wang, W. Zhou, H. Liu, Y. Sang, Suppressing Photoinduced Charge Recombination via the Lorentz Force in a Photocatalytic System, Adv. Sci., 6 (2019) 1901244, https://doi.org/10.1002/advs.201901244.

[42] X. Li, W. Wang, F. Dong, Z. Zhang, L. Han, X. Luo, J. Huang, Z. Feng, Z. Chen, G. Jia, T. Zhang, Recent Advances in Noncontact External-Field-Assisted Photocatalysis: From Fundamentals to Applications, ACS Catal., 11 (2021) 4739-4769, https://doi.org/10.1021/acscatal.0c05354.

[43] X. Wang, S.O. Pehkonen, J. Rämö, M. Väänänen, J.G. Highfield, K. Laasonen, Experimental and computational studies of nitrogen doped Degussa P25 $TiO_2$: application to visible-light driven photo-oxidation of As(iii), Catal. Sci. Technol., 2 (2012) 784-793, https://doi.org/10.1039/C2CY00486K.

[44] T. Luo, S. Abdu, M. Wessling, Selectivity of ion exchange membranes: A review,

J. Membr. Sci., 555 (2018) 429-454, https://doi.org/10.1016/j.memsci.2018.03.051.

[45] G. Leofanti, M. Padovan, G. Tozzola, B. Venturelli, Surface area and pore texture of catalysts, Catal. Today, 41 (1998) 207-219, https://doi.org/10.1016/S0920-5861(98)00050-9.

[46] W. Tang, Z. Ren, X. Lu, S. Wang, Y. Guo, S. Hoang, S. Du, P.-X. Gao, Scalable integration of highly uniform $Mn_xCo_{3-x}O_4$ nano-sheet array onto ceramic monolithic substrates for low temperature propane oxidation, ChemCatChem, 9 (2017) 4112-4199. https://doi.org/10.1002/cctc.201700795.

[47] S. Bernardini, F. Bellatreccia, A. Casanova Municchia, G. Della Ventura, A. Sodo, Raman spectra of natural manganese oxides, J. Raman Spectrosc, 50 (2019) 873-888, https://doi.org/10.1002/jrs.5583.

[48] L. Zhang, Y. Liu, S. Wang, B. Liu, J. Peng, Selective removal of cationic dyes from aqueous solutions by an activated carbon-based multicarboxyl adsorbent, RSC Adv., 5 (2015) 99618-99626, https://doi.org/10.1039/C5RA18093G.

[49] B.H. Hameed, A.A. Ahmad, N. Aziz, Isotherms, kinetics and thermodynamics of acid dye adsorption on activated palm ash, Chem. Eng. J., 133 (2007) 195-203, https://doi.org/10.1016/j.cej.2007.01.032.

[50] F.-C. Wu, R.-L. Tseng, R.-S. Juang, Comparative adsorption of metal and dye on flake- and bead-types of chitosans prepared from fishery wastes, J. Hazard. Mater., 73 (2000) 63-75, https://doi.org/10.1016/S0304-3894(99)00168-5.

[51] K.G. Bhattacharyya, A. Sharma, Adsorption of Pb(II) from aqueous solution by Azadirachta indica (Neem) leaf powder, J. Hazard. Mater., 113 (2004) 97-109,

https://doi.org/10.1016/j.jhazmat.2004.05.034.

[52] L. Xiong, Y. Yang, J. Mai, W. Sun, C. Zhang, D. Wei, Q. Chen, J. Ni, Adsorption behavior of methylene blue onto titanate nanotubes, Chem. Eng. J., 156 (2010) 313-320, https://doi.org/10.1016/j.cej.2009.10.023.

[53] L. Li, S. Liu, T. Zhu, Application of activated carbon derived from scrap tires for adsorption of Rhodamine B, J Environ Sci (China), 22 (2010) 1273-1280, https://doi.org/10.1016/S1001-0742(09)60250-3.

[54] X. Lei, X. Li, Z. Ruan, T. Zhang, F. Pan, Q. Li, D. Xia, J. Fu, Adsorption-photocatalytic degradation of dye pollutant in water by graphite oxide grafted titanate nanotubes, J. Mol. Liq., 266 (2018) 122-131, https://doi.org/10.1016/j.molliq.2018.06.053.

[55] C.H. Giles, A.P. D'Silva, I.A. Easton, A general treatment and classification of the solute adsorption isotherm part. II. Experimental interpretation, J. Colloid Interface Sci., 47 (1974) 766-778, https://doi.org/10.1016/0021-9797(74)90253-7.

[56] C.H. Giles, T.H. MacEwan, S.N. Nakhwa, D. Smith, 786. Studies in adsorption. Part XI. A system of classification of solution adsorption isotherms, and its use in diagnosis of adsorption mechanisms and in measurement of specific surface areas of solids, J. Chem. Soc., (1960) 3973-3993, https://doi.org/10.1039/JR9600003973.

[57] L.V. Gritsenko, K.A. Abdullin, M.T. Gabdullin, Z.K. Kalkozova, S.E. Kumekov, Z.O. Mukash, A.Y. Sazonov, E.I. Terukov, Effect of thermal annealing on properties of polycrystalline ZnO thin films, J. Cryst. Growth, 457 (2017) 164-170, https://doi.org/10.1016/j.jcrysgro.2016.07.026.

[58] Y. Liu, Q. Zhang, H. Yuan, K. Luo, J. Li, W. Hu, Z. Pan, M. Xu, S. Xu, I. Levchenko, K. Bazaka, Comparative study of photocatalysis and gas sensing of ZnO/Ag nanocomposites synthesized by one- and two-step polymer-network gel processes, J. Alloys Compd., 868 (2021) 158723, https://doi.org/10.1016/j.jallcom.2021.158723.

[59] X. Li, B. Kang, F. Dong, Z. Zhang, X. Luo, L. Han, J. Huang, Z. Feng, Z. Chen, J. Xu, B. Peng, Z.L. Wang, Enhanced photocatalytic degradation and $H_2/H_2O_2$ production performance of S-pCN/$WO_{2.72}$ S-scheme heterojunction with appropriate surface oxygen vacancies, Nano Energy, 81 (2021) 105671, https://doi.org/10.1016/j.nanoen.2020.105671.

[60] X. Li, J. Xiong, X. Gao, J. Ma, Z. Chen, B. Kang, J. Liu, H. Li, Z. Feng, J. Huang, Novel BP/BiOBr S-scheme nano-heterojunction for enhanced visible-light photocatalytic tetracycline removal and oxygen evolution activity, J. Hazard. Mater., 387 (2020) 121690, https://doi.org/10.1016/j.jhazmat.2019.121690.

[61] J. Xiong, X. Li, J. Huang, X. Gao, Z. Chen, J. Liu, H. Li, B. Kang, W. Yao, Y. Zhu, CN/rGO@BPQDs high-low junctions with stretching spatial charge separation ability for photocatalytic degradation and $H_2O_2$ production, Appl. Catal. B, 266 (2020) 118602, https://doi.org/10.1016/j.apcatb.2020.118602.

[62] J.-P. Zou, Y. Chen, M. Zhu, D. Wang, X.-B. Luo, S.-L. Luo, 2 - Semiconductor-Based Nanocomposites for Photodegradation of Organic Pollutants, in: X. Luo, F. Deng (Eds.) Nanomaterials for the Removal of Pollutants and Resource Reutilization, Elsevier, 2019, pp. 25-58,

https://doi.org/10.1016/B978-0-12-814837-2.00002-0.

[63] M. Oku, H. Matsuta, K. Wagatsuma, Y. Waseda, S. Kohiki, Removal of inelastic scattering part from Ti2p XPS spectrum of $TiO_2$ by deconvolution method using O1s as response function, J. Electron Spectrosc. Relat. Phenom., 105 (1999) 211-218, https://doi.org/10.1016/S0368-2048(99)00067-5.

[64] L. Lin, Y. Ma, J. Wu, F. Pang, J. Ge, S. Sui, Y. Yao, R. Qi, Y. Cheng, C.-g. Duan, J. Chu, R. Huang, Origin of Photocatalytic Activity in $Ti^{4+}/Ti^{3+}$ Core–Shell Titanium Oxide Nanocrystals, J. Phys. Chem. C, 123 (2019) 20949-20959, https://doi.org/10.1021/acs.jpcc.9b05285.

[65] H. She, H. Zhou, L. Li, L. Wang, J. Huang, Q. Wang, Nickel-Doped Excess Oxygen Defect Titanium Dioxide for Efficient Selective Photocatalytic Oxidation of Benzyl Alcohol, ACS Sustain. Chem. Eng., 6 (2018) 11939-11948, https://doi.org/10.1021/acssuschemeng.8b02217.

[66] J.-C. Dupin, D. Gonbeau, P. Vinatier, A. Levasseur, Systematic XPS studies of metal oxides, hydroxides and peroxides, Phys. Chem. Chem. Phys., 2 (2000) 1319-1324, https://doi.org/10.1039/A908800H.

[67] Z. Wei, D. Liu, W. Wei, X. Chen, Q. Han, W. Yao, X. Ma, Y. Zhu, Ultrathin $TiO_2$(B) Nanosheets as the Inductive Agent for Transfrering $H_2O_2$ into Superoxide Radicals, ACS Appl. Mater. Interfaces, 9 (2017) 15533-15540, https://doi.org/10.1021/acsami.7b03073.

[68] E. Carter, A.F. Carley, D.M. Murphy, Evidence for $O^{2-}$ Radical Stabilization at Surface Oxygen Vacancies on Polycrystalline $TiO_2$, J. Phys. Chem. C, 111 (2007)

10630-10638, https://doi.org/10.1021/jp0729516.

[69] J. Chen, Z. Zhang, W. Zhu, L. Zhang, B. Zhao, Y. Ji, G. Li, T. An, Superoxide radical enhanced photocatalytic performance of styrene alters its degradation mechanism and intermediate health risk on $TiO_2$/graphene surface, Environ. Res., 195 (2021) 110747, https://doi.org/10.1016/j.envres.2021.110747.

[70] Y.-Y. Yang, X.-G. Zhang, C.-G. Niu, H.-P. Feng, P.-Z. Qin, H. Guo, C. Liang, L. Zhang, H.-Y. Liu, L. Li, Dual-channel charges transfer strategy with synergistic effect of Z-scheme heterojunction and LSPR effect for enhanced quasi-full-spectrum photocatalytic bacterial inactivation: new insight into interfacial charge transfer and molecular oxygen activation, Appl. Catal. B, 264 (2020) 118465, https://doi.org/10.1016/j.apcatb.2019.118465.

[71] C. Liang, H.-Y. Niu, H. Guo, C.-G. Niu, Y.-Y. Yang, H.-Y. Liu, W.-W. Tang, H.-P. Feng, Efficient photocatalytic nitrogen fixation to ammonia over bismuth monoxide quantum dots-modified defective ultrathin graphitic carbon nitride, Chem. Eng. J., 406 (2021) 126868, https://doi.org/10.1016/j.cej.2020.126868.

[72] J. Yang, J. You, J. Dai, Y. Chen, Y. Li, In-Situ Synthesis of Hydrogen Titanate Nanotube/Graphene Composites with a Chemically Bonded Interface and Enhanced Visible Photocatalytic Activity, Nanomaterials, 8 (2018) 229; https://doi.org/10.3390/nano8040229.

[73] T. Raguram, K.S. Rajni, Synthesis and analysing the structural, optical, morphological, photocatalytic and magnetic properties of $TiO_2$ and doped (Ni and Cu) $TiO_2$ nanoparticles by sol–gel technique, Appl. Phys. A, 125 (2019) 288,

https://doi.org/10.1007/s00339-019-2581-1.

[74] C. Yan, K.-F. Chen, C.-H. Lai, S.-W. Lai, Q. Chang, Y.-P. Peng, Photocatalytic degradation of Rhodamine B by microwave-assisted hydrothermal synthesized N-doped titanate nanotubes, J Environ Sci (China), 26 (2014) 1505-1512, https://doi.org/10.1016/j.jes.2014.05.017.

[75] H.-Y. Liu, C. Liang, C.-G. Niu, D.-W. Huang, Y.-B. Du, H. Guo, L. Zhang, Y.-Y. Yang, G.-M. Zeng, Facile assembly of g-$C_3N_4$/$Ag_2CO_3$/graphene oxide with a novel dual Z-scheme system for enhanced photocatalytic pollutant degradation, Appl. Surf. Sci., 475 (2019) 421-434, https://doi.org/10.1016/j.apsusc.2019.01.018.

[76] Y.-Y. Yang, C.-G. Niu, X.-J. Wen, L. Zhang, C. Liang, H. Guo, D.-L. Guan, H.-Y. Liu, G.-M. Zeng, Fabrication of visible-light-driven silver iodide modified iodine-deficient bismuth oxyiodides Z-scheme heterojunctions with enhanced photocatalytic activity for Escherichia coli inactivation and tetracycline degradation, J. Colloid Interface Sci., 533 (2019) 636-648, https://doi.org/10.1016/j.jcis.2018.09.008.

[77] H. Guo, C.-G. Niu, C.-Y. Feng, C. Liang, L. Zhang, X.-J. Wen, Y. Yang, H.-Y. Liu, L. Li, L.-S. Lin, Steering exciton dissociation and charge migration in green synthetic oxygen-substituted ultrathin porous graphitic carbon nitride for boosted photocatalytic reactive oxygen species generation, Chem. Eng. J., 385 (2020) 123919, https://doi.org/10.1016/j.cej.2019.123919.

[78] R. Ashiri, Detailed FT-IR spectroscopy characterization and thermal analysis of synthesis of barium titanate nanoscale particles through a newly developed process, Vib. Spectrosc., 66 (2013) 24-29, https://doi.org/10.1016/j.vibspec.2013.02.001.

[79] W. Kang, Y. Gao, X. Tang, C. Cao, L. Hu, H. Yang, Polymer concentration detection method based on fluorescent polymer to evaluate its retention and percolation, J. Appl. Polym. Sci., 136 (2019) 47468, https://doi.org/10.1002/app.47468.

[80] S. Requena, S. Lacoul, Y.M. Strzhemechny, Luminescent Properties of Surface Functionalized $BaTiO_3$ Embedded in Poly(methyl methacrylate), Materials, 7 (2014) 471-483, https://doi.org/10.3390/ma7010471.

[81] H. Guo, H.-Y. Niu, C. Liang, C.-G. Niu, Y. Liu, N. Tang, Y. Yang, H.-Y. Liu, Y.-Y. Yang, W.-J. Wang, Few-layer graphitic carbon nitride nanosheet with controllable functionalization as an effective metal-free activator for peroxymonosulfate photocatalytic activation: Role of the energy band bending, Chem. Eng. J., 401 (2020) 126072, https://doi.org/10.1016/j.cej.2020.126072.

[82] L. Li, C.-G. Niu, H. Guo, J. Wang, M. Ruan, L. Zhang, C. Liang, H.-Y. Liu, Y.-Y. Yang, Efficient degradation of Levofloxacin with magnetically separable $ZnFe_2O_4$/NCDs/$Ag_2CO_3$ Z-scheme heterojunction photocatalyst: Vis-NIR light response ability and mechanism insight, Chem. Eng. J., 383 (2020) 123192, https://doi.org/10.1016/j.cej.2019.123192.

[83] H.-Y. Liu, C.-G. Niu, H. Guo, C. Liang, D.-W. Huang, L. Zhang, Y.-Y. Yang, L. Li, In suit constructing 2D/1D $MgIn_2S_4$/CdS heterojunction system with enhanced photocatalytic activity towards treatment of wastewater and $H_2$ production, J. Colloid Interface Sci., 576 (2020) 264-279, https://doi.org/10.1016/j.jcis.2020.05.025.